Response to Anonymous Reviewer #1

May 15, 2015

The authors are very grateful to the anonymous reviewer for all of their helpful comments and suggestions. The comments are fair, reasonable and contribute to the improvement of the paper.

1 Major Comment

Reviewer's Comment: I have found that the authors provide convincing arguments that the broad longitudinal enhancement of gravity wave activity is likely to be associated with a nearly uniform gravity-wave source at 60°S. In particular, I think that it is quite unlikely that the Andes and Antarctic Peninsula could generate waves with horizontal wavelengths much longer than 350 km, and thus significantly contribute to the gravity-wave activity enhancement east of 20E. On the other hand, I am less convinced by the authors claim (in particular around p3185 l13-26; p3199, l9-16; p3200 last paragraph and p3201 first paragraph) that Figure 4 supports that this broad gravity-wave source is likely to be a local stratospheric source (either secondary generation from primary mountain waves or stratospheric jet adjustment or instabilities). I have mainly two reservations:

- first, the fact that Figure 4 shows that Ep peaks around 20-35 km in August above the Austral Ocean (letting apart the orographic waves at 60W) may result from an observational effect associated with the GPS-RO dataset. As shown on Figure 3, the zonal wind increases from the tropopoause to 35 km at 60°S in August, which will result in an increase of the vertical wavelength of westward propagating gravity waves. Some of these waves may thus be invisible in the GPS-RO dataset below 20km (vertical wavelength less than twice the GPS-RO vertical resolution, i.e., 2.8km), but become more and more resolved as the wind increases above. OSullivan and Dunkerton (1995) for instance show that waves generated around the tropospheric jet have vertical wavelengths of a few kilometers. The maps on Figure 2 are furthermore much reminiscent of the spiral structure of the Southern Hemisphere storm track with less activity over the Pacific Ocean (see, e.g., Hoskins and Hodges (2005)), so that this broad gravity-wave feature may actually be associated with non-orographic waves generated in the tropopsphere.

  Authors' Response: Agreed. We have updated the article such that we discuss this effect in our description of Figure 4 in Section 2.3 and the main discussion in Section 5. We include relevant references to O'Sullivan and Dunkerton (1995) and Hoskins and Hodges (2005) as suggested.

  Reviewer's Comment: then, it is written in the article that the quantity displayed on Figure 4 (and Figure 3) has been normalized, but this normalization has not been explicited. Raw $E - p$ is not density weighted (cf. Eq. (3)), so that it is expected to increase as exp(z/H) for linear waves, with H the density-scaled height. Is the normalization used by the authors supposed to counterbalance this increase? Otherwise, one can not deduce from the peak of E_p at 30 km on Figure 4 that it is associated with a local source: it may rather be the altitude where gravity waves generated below deposit most of their momentum. I therefore strongly suggest that the authors present a explicitly density-weighted version of Figure 4, so that one will be able to assess where the waves observed above the oceans are primarily generated.

  Authors' Response: For each height level in Figures 3 and 4, E_p is normalised such that the lowest value is equal to 0 and the highest value is equal to 1. This normalisation identifies the relative intensity of E_p in the panel at each height level and removes any exponential increase with decreasing pressure. This is the same normalisation as was used by Wright and Gille (2011, their Figure 4). This normalisation approach already accounts for decreasing density. We have updated the description of the normalisation to make this clearer.

2 Minor Comments

- **p.3178, l.25:** ***Reviewer's Comment:*** (and p3179, l2): Actually, waves with $\lambda_H < 2 \times 270\,\mathrm{km}$ are unlikely to be detected (Nyquist wavelength).

  Authors' Response: We do not agree, see Kursinski et al. (1997, Section 2.5). Nyquist-sampling limitations only apply to the vertical profile. The horizontal resolution of each data point in the vertical profile is determined by an integral along the line-of-sight and is not Nyquist-sampled. An alternative discussion of

the horizontal resolution of a limb-sounding instrument using a line-of-sight integral method can be found in Preusse et al. (2002, 2009).

- **p.3179, l.2-7:** ***Reviewer's Comment:*** It is recalled here that most of the orographic waves generated above the Andes or by the Antarctic Peninsula have "westward oriented horizontal wavenumber vectors", while the "COSMIC occultations in this region tend to be preferentially aligned towards the north-south axis". I would like that the authors further develop this point, and in particular discuss how it could affect the sensitivity of the measurements to wave disturbances. One issue that strikes me for instance is that the HIRDLS soundings are performed in a direction almost perpendicular to the GPS occultations in this region. I thus wonder what is the meaning of the comparisons performed in section 4: how can both techniques be sensitive to the same waves there? Which technique is the best suited to obaserve zonally propagating waves in this region? And what is the validity of λ_H derived from the GPS RO there?

  Authors' Response: We do not claim that HIRDLS and COSMIC are sensitive to exactly the same waves, although their observational filters should be similar. As mentioned in Section 1, the COSMIC horizontal line of sight (LOS) resolution is ∼270 km. The average theoretical horizontal resolution along the axis joining the profile-pairs used in Section 4 is $\sim 2 \times \Delta r = 20\,km$. A sensible value for the HIRDLS LOS resolution is ∼300 km (e.g. Presse et al., 2009 and citations therein). The HIRDLS along-track resolution is twice the inter-profile spacing, up to $\sim 2 \times \Delta r = 160$ or 240 km (there are generally two values of Δr for HIRDLS, see Appendix A). If a wave in this region has a true absolute horizontal wavelength greater than ∼300 km, it should be detected by both COSMIC and HIRDLS, regardless of orientation. There is a very large overlap in the observational filters of both instruments, and the two are broadly comparable in the horizontal domain. We acknowledge that differences may arise in special cases where wavefronts are aligned favourably for one instrument such that it may resolve a wave with $\lambda_H < 300$ km when the other instrument may not. We are confident however that differences arising from this effect are not significant in the general case and do not undermine our comparison in Section 4. The north-south GPS-RO LOS orientation is favourable for the detection of zonally propagating waves with true absolute horizontal wavelength slightly shorter than 270 km (see also later response below).

- **p.3181-3182, l.29-5:** ***Reviewer's Comment:*** I also observe on Figure 2 that one does not observe a continuous decrease of E_p as one goes farther East in the "leeward" region of increased E_p. This seems to be in contradiction that most of these waves are of orographic origin. On the other hand, your discussion here seems to make the implicit assumption that the waves were generated above the mountains and "have long dwell times".

  Authors' Response: We do not claim that most of the waves in the long leeward distribution of increased E_p are of orographic origin. Sato et al. (2012) suggested that some of this feature could be explained by the leeward advection of mountain waves from the southern Andes and Antarctic Peninsula. Their ray-tracing analysis suggested however that the increased E_p eastward of around 20°E is not likely to be explained by this mechanism. The term "long dwell times" refers to the relatively low vertical group velocity of low-frequency inertia-gravity waves relative to their high-frequency counterparts (Fritts and Alexander, 2003). These waves "dwell" longer in the atmosphere, increasing their likelihood of detection by a pseudo-random sampling technique such as GPS-RO. The vertical and horizontal observational filters of GPS-RO (roughly $5 < \lambda_Z < 15$ km and $\lambda_H > 270$ km) favour detection of these low-frequency waves.

- **p.3183, l.28-29:** ***Reviewer's Comment:*** You may recall here to which altitude range does this 2500 km horizontal propagation distance correspond?

  Authors' Response: This horizontal propagation distance is traversed whilst the simulated waves ascend from the ground to 40 km. The horizontal propagation distance approximate since Sato et al. launched a number of waves that traversed different distances for different launch angles and latitudes.

- **p.3184, l.6-9:** ***Reviewer's Comment:*** This is actually somewhat striking that the Antarctic Peninsula does not show up very clearly in your dataset, while it has been recognized as a major hotspot by several previous studies. Could you discuss whether this could be an effect of the RO orientation at high latitudes, or if it is due to the vertical wavelength range in which the GPS RO are most sensitive?

  Authors' Response: The Antarctic Peninsula shows up as a major hot spot in our results, as is evident in Figure 10c. This paragraph in question relates to the lack of a symmetric meridional focussing effect so clear as was observed over the Andes in Figure 3, not the lack of waves over the Antarctic Peninsula itself.

- **p.3187, l.1:** ***Reviewer's Comment:*** p3187, l1: Is this normalization really needed?

  Authors' Response: Yes this normalisation is absolutely necessary. Otherwise it is not possible to set one consistent threshold value for $C_{\max}$ to be applied to every profile. We have re-written the description of this section of the Wave-ID method description in response to another reviewer, and we hope that the reasoning behind each step is clearer.

- **p.3188, l.2:** ***Reviewer's Comment:*** p3188 l2: unless I have missed something, this 1 K lower and 10 K upper limits appear here for the first time without real justification. Do you use the lower limit to avoid including noise in your analysis? Why do you need an upper limit? How sensitive are your results if you change these limits?

  Authors' Response: The estimated accuracy of COSMIC GPS-RO temperature profiles is generally $\sim$1 K or better (e.g. Tsuda et al., 2011 and citations therein). It is very unlikely therefore that we can reliably disassociate waves with amplitude $T' < 1$ K with noise related to the RO retrieval or improper background temperature removal. We take $T' > 1$ K as a reasonable lower limit. Resolved gravity waves of these scales with amplitudes $T' > 10$ K are rare in satellite data. We believe amplitudes this large in the level 2 COSMIC retrieval are more likely to be spikes related to error or miscalibration in the retrieval than real gravity waves. Furthermore, such large amplitudes fall well outside the 95^{th} percentile of the amplitude distributions in Figure 9. It is for this reason that we set the upper limit to $T' < 10$ K.

- **p.3189, l.20:** ***Reviewer's Comment:*** I would add "detected by the wave 1D method" between "waves" and "themselves".

  Authors' Response: Agreed, changed.

- **p.3190, l.2-8:** ***Reviewer's Comment:*** Both sentences have very similar meaning.

  Authors' Response: Agreed, though there is a subtle but important difference. The fact that the peak of the distribution shifts implies large amplitude, highly intermittent waves in the vicinity of the peak. The fact that the rest of the distribution does not move implies that the rest of the distribution is made up of waves which are not as intermittent. We have rephrased the paragraph to highlight this difference.

- **p.3191, l.17:** ***Reviewer's Comment:*** typo: $3 < T'$

  Authors' Response: Corrected.

- **p.3194, l.20:** ***Reviewer's Comment:*** See remarks p.3179 l.2-7: Is the RO orientation not too problematic here, as the waves are expected to be mostly zonally propagating?

  Authors' Response: The phase-fronts of zonally propagating waves will be aligned roughly parallel to the north-south axis. This means that the horizontal wavelength in the north-south direction can be very long. This favours detection by COSMIC occultations with north-south alignment, since we require $\lambda_H > 270$ km in the line-of-sight. The estimation of λ_H used in Section 4 is the component of λ_H projected along the axis joining the two profiles in a profile-pair. This axis is often roughly perpendicular to the line-of-sight. The cross-beam resolution of GPS-RO is $\sim$1.4 km (Kursinski et al., 1997), so we can even (theoretically, see Appendix A) resolve zonally propagating waves with very short horizontal wavelength components in the east-west direction. In summary, the orientation of RO profiles here is actually favourable to the detection of zonally propagating waves.

- **Figure 11** ***Reviewer's Comment:*** could you label the longitudes on this plot? Why are you limiting these maps to the South America sector?

  Authors' Response: We assume the reviewer means Figure 10. The longitudes are labelled on panel (f) of Figure 10. Each map has the same geographical extent, and the addition of repeated longitude labels on each panel leads to significant visual clutter which detracts from easy interpretation of the results.

In addition to the changes requested by the reviewers, we have also made some small changes to the structure of the abstract, introduction and conclusions, with the aim of providing a better scientific context for the work undertaken.

3 References

Fritts, D. C. and Alexander, M. J.: Gravity wave dynamics and effects in the middle atmosphere, Rev. Geophys., 41, 1003, doi:10.1029/2001RG000106, 2003.

Kursinski, E. R., Hajj, G. A., Schofield, J. T., Linfield, R. P., and Hardy, K. R.: Observing Earths atmosphere with radio occultation measurements using the Global Positioning System, J. Geophys. Res., 102, 2342923465, doi:10.1029/97JD01569, 1997.

Preusse, P., Doernbrack, A., and Eckermann, S.: Space-based measurements of stratospheric mountain waves by CRISTA 1. Sensitivity, analysis method, and a case study, J. Geophys. Res., 107, 8178, doi:10.1029/2001JD000699, 2002.

Preusse, P., Schroeder, S., Hoffmann, L., Ern, M., Friedl-Vallon, F., Ungermann, J., Oelhaf, H., Fischer, H., and Riese, M.: New perspectives on gravity wave remote sensing by spaceborne infrared limb imaging, Atmospheric Measurement Techniques, 2, 299311, doi:10.5194/amt-2-299-2009, 2009.

Sato, K., Watanabe, S., Kawatani, Y., Tomikawa, Y., Miyazaki, K., and Takahashi, M.: On the origins of mesospheric gravity waves, Geophys. Res. Lett., 36, L19801, doi:10.1029/2009GL039908, 2009.

Tsuda, T., Lin, X., Hayashi, H., and Noersomadi: Analysis of vertical wave number spectrum of atmospheric gravity waves in the stratosphere using COSMIC GPS radio occultation data, Atmos. Meas. Tech., 4, 16271636, doi:10.5194/amt-4-1627-2011, 2011.

Yan, X., Arnold, N., and Remedios, J.: Global observations of gravity waves from High Resolu- tion Dynamics Limb Sounder temperature measurements: a year-long record of temperature amplitude, J. Geophys. Res., 115, D10113, doi:10.1029/2008JD011511, 2010.

Response to Anonymous Reviewer #2

May 15, 2015

The authors are very grateful to the anonymous reviewer for all of their helpful comments and suggestions. The comments are fair, reasonable and contribute to the improvement of the paper.

1 Major Comments

- **(MC1)** ***Reviewer's Comment:*** More discussion is needed regarding the vertical wavelength limitations of the analysis method. Otherwise it cannot be decided whether features of the gravity wave distribution are caused by the analysis technique, or whether they are an effect of gravity wave propagation. This concern is addressed in more detail in the specific comments, particularly in specific comment 7.

  Authors' Response: Agreed. We have provided more discussion on the vertical wavelength sensitivity of our analysis method in Section 2.2 and elsewhere. See our response to specific comment 7.

- **(MC2)** ***Reviewer's Comment:*** Horizontal separations of altitude profiles as short as 10-20km are used for determining horizontal wavelengths. This is quite short and will lead to random effects. This may explain some of the differences between HIRDLS and COSMIC in Fig. 10. Fig. 10 should be revised by using longer horizontal separations. See also specific comments 16, 17 and 21.

  Authors' Response: Agreed. We have included Appendix A to investigate the precise effect of these short horizontal separations on our estimation of λ_H. It is not possible to revise Figure 10 using only longer horizontal separations. There are too few COSMIC profile-pairs with which to draw useful statistics if we exclude pairs with short horizontal separations (see Figure 11). We present results from the largest dataset we have available and discuss biases that may be introduced as a result. See also responses to specific comments 16,17 and 21.

2 Specific Comments

1. **p.3175, l.4:** ***Reviewer's Comment:*** For completeness, the earlier reference Eckermann and Preusse (1999) should be included.

   Authors' Response: Reference to Eckermann and Preusse (1999) included as requested.

2. **p.3179, l.26:** ***Reviewer's Comment:*** It should be pointed out more clearly that at this stage of calculating E_p the blue dashed curve in Fig. 6 applies, and a certain contribution of $\lambda_Z > 10\,\mathrm{km}$ is still contained in T'. This is important because later, when discussing Fig. 3, it is claimed that meridional propagation of gravity waves would be seen. Assuming a sharp cutoff at λ_Z=10km, mountain waves would become invisible if the background wind U parallel to the wave vector exceeds $\sim$30 m/s. For mountain waves: $\lambda_Z \approx 2\pi U/N$ (Eckermann and Preusse, 1999, Eq. 1)

   Authors' Response: We have revised this section to include a better description of the vertical scales to which our analysis is sensitive. There is in fact no sharp cut-off at $\lambda_Z = 10\,\mathrm{km}$. Indeed, as the reviewer suggests, the analysis method is predominantly sensitive to waves with $\sim 3 < \lambda_Z < 14\,\mathrm{km}$, though wavelengths greater than $\sim$10 km will be suppressed by some factor.

3. **p.3180, l.55:** ***Reviewer's Comment:*** It is unclear why the gravity wave distribution consisting of more or less randomly distributed temperature fluctuations should be affected by removing coherent planetary scale waves with s=1 or s=2. Please explain!

   Authors' Response: Sentence deleted.

4. **p.3180, l.23-24:** ***Reviewer's Comment:*** Why should a 10km window further reduce contributions of planetary waves? If T at a fixed altitude is affected by planetary waves, this planetary wave contribution will enter E_p, independent of the size of the window. Further reduction of planetary waves can only be achieved by separately removing the offset in every 10km window. This is however not mentioned. Please either explain or delete this sentence.

   Authors' Response: Agreed, sentence deleted. We use a single 10 km vertical averaging window at a single point, not a sliding 10 km window along the whole profile.

5. **p.3181, l.28:** ***Reviewer's Comment:*** The reduced sensitivity for gravity waves directly over the mountain ridges is not only an effect of the GPS-RO observation technique. The data analysis technique plays also an important role! Depending on the strength of the background wind, vertical wavelengths of mountain waves can be quite long. These long λ_Z waves should be contained in the GPS-RO temperature altitude profiles and can therefore be detected. Also other limb observations with similar observational filter show maximum gravity wave variances over the mountains (for example, Yan et al., 2010). Possibly, the vertical wavelength limitation in your study to only short λ_Z reduces the sensitivity to mountain waves, and may in some regions favor waves from sources other than orography. It should therefore be mentioned that increased E_p over the Southern Ocean could be just an effect of the analysis technique that is limited to short λ_Z waves.

   Authors' Response: We have updated this section to reflect the reviewer's comments. Our filtering method does not preclude the detection of longer λ_Z waves directly over the mountains, only underestimates their amplitude. We do acknowledge that this is likely the reason for the differing distributions from other studies such as Yan et al. (2010), and we have updated the article to reflect this.

6. **p.3182, l.9:** ***Reviewer's Comment:*** Please omit "significant "; up to 10% is not a large fraction.

   Authors' Response: Omitted as suggested.

7. **p.3183, ll.13ff / discussion of Fig. 3:** ***Reviewer's Comment:***

   The background wind in the southern polar jet can be quite strong. It is up to 80 m/s in Fig. 3, and it changes a lot from 40S/22km and 20 m/s to 55S/40km and 70 m/s. Therefore it could be doubted that mountain waves are captured by your analysis over the whole range of altitudes and latitudes considered. A discussion of observational effects related to the vertical wavelength range of your analysis should therefore be included in the manuscript. In addition, previous work that supports your findings should be mentioned. Please find below a suggested roadmap for this additional discussion:

   - $\lambda_Z \approx 2\pi U/N$ (Eckermann and Preusse, 1999, Eq. 1): therefore it might be doubted that mountain waves are captured by your analysis for background winds stronger than 40-50 m/s, taking into account the limited vertical wavelength coverage.
   - Still, your analysis will capture mountain waves for even stronger background winds because the background wind vector and the wave vector of the gravity waves will not be exactly parallel (for example, Alexander and Teitelbaum, 2011)
   - This is further supported by vertical wavelength observations in the southern polar jet from analyses with larger vertical wavelength coverage. On zonal average, these estimates are in the range 1013 km (for example, Yan et al., 2010; Ern et al., 2011).
   - Therefore the slanted vertical column of enhanced Ep in Fig. 3 could be due to mountain waves and could indicate meridional propagation.
   - Similar effects have been observed before in other regions (for example Jiang et al., 2004; Ern et al., 2013)

   Authors' Response: We are grateful to the reviewer for their comments and suggested roadmap for revision. We have included a paragraph in the paper discussing the points raised around Figure 3.

8. **p.3184, ll.11-14:** ***Reviewer's Comment:*** Which latitudes are considered for the zonal cross-section? The range is given in the figure caption, but should also be given here.

   Authors' Response: Latitude range included as suggested.

9. **p.3187, ll.18-19:** ***Reviewer's Comment:*** p.3187, ll.18/19: "at least 60% of the root-sum-squared energy of the profile" Is this correct? Shouldn't it read "at least 60% of the spectral amplitude..."? Please check!

   Authors' Response: We have revised Section 3.1 to provide an improved description of the properties involved with the Wave-ID methodology. Instead of fraction RSS energy, the output of the CWT can be roughly interpreted as a map of pseudo-correlation coefficients between the profile and the analysing wavelet, provided both have RSS energy equal to one and both are zero-averaged. This means we are able to move away from the rather confusing description fractions of RSS energy as described in the discussion paper. The methodology, figures and results remain unchanged, only the description of the parameters involved has been improved. To answer the reviewer's specific question, we did mean "at least 60% of the root-sum-square energy of the profile".

10. **p.3187, ll.17ff:** ***Reviewer's Comment:*** Does a squared spectral amplitude threshold of 0.36 / spectral amplitude threshold of 0.6 imply that at a given altitude usually only one wave is selected? Or are multiple selections possible? This information should be included in the manuscript.

    Authors' Response: We currently limit this methodology to detecting one (the dominant) wave per profile. This information has been included at the end of Section 3.1.

11. **p.3187/8,** ***Reviewer's Comment:*** The following should be mentioned: It is assumed that the vertical wavelength does not change much with altitude, which may no longer hold for gravity waves in the real atmosphere if the width of the wavelet gets too large. In particular, long vertical wavelength waves will therefore be selected with lower probability. This may explain the slight mismatch between the histogram in Fig. 6 and the "permitted" range of vertical wavelengths given by the black curve.

    Authors' Response: We have included this suggestion and the implicit limitation of the method at the end of Section 3.1.

12. **p.3189, l.23 and elsewhere:** ***Reviewer's Comment:*** The statement "profiles that did not contain a wave" is too strong, given the limitations of the analysis method. Perhaps replace with "profiles with no wave detected".

    Authors' Response: Replaced as suggested.

13. **p.3190, l.15:** ***Reviewer's Comment:*** Sector C has quite large longitudinal extent. It would be good to add a sector C', $\sim 1/3$ of the longitude extent of C, thereby focusing more on the vicinity of the Drake Passage where "primary mountain waves" should cause even higher intermittency.

    Authors' Response: Adding another small sector to focus on the Drake Passage region would indeed be of interest, however a number of difficulties exist with regard to including it in the figure, mainly relating to the charge requiring an otherwise-unnecessary normalisation of the data.We have run the analysis on a small sector from 80W-60W in the latitude band. The resulting histogram is very similar to Sector C but as the reviewer suggests, a very slightly bias towards larger amplitude waves is evident, possibly consistent with intermittent mountain wave activity. This effect is quite small however.

14. **Figure 9** ***Reviewer's Comment:*** In this figure both the number of waves and the number of profiles are indicated below the histograms. Calculating the ratio of these numbers, the fraction of profiles containing an identified wave is around 80%. This is in discrepancy with the number of 25-40% mentioned on p.3188, l.5. Please check and clarify!

    Authors' Response: The 25-40% value on p.3188, l.5 is a global, all-year average. During June-August, in the latitude band 40S-65S, the fraction of profiles in which wave-like features were identified is significantly increased, as the reviewer calculates up to $\sim 80\%$. We agree that the sentence on p.3188 is not clear enough. We have replaced it with "we find that on global year-long average around 25-40% of profiles contain an indentifiable gravity wave signal. In some regions and seasons, as will be seen later, this fraction can be as high as $\sim 80\%$."

15. **p.3193, l.8:** ***Reviewer's Comment:*** p.3193, l.8: Please mention that k_h has previously been determined by McDonald (2012) and by Faber et al. (2013) using pairs of COSMIC radio occultations.

    Authors' Response: References added as suggested.

16. **p.3193, l.22/33ff:** ***Reviewer's Comment:*** Horizontal separations as short as 10-20 km are probably too short to reliably determine k_h. Estimated horizontal wavelengths of 1000 km for gravity waves are quite common in satellite data, as seen in your Fig. 10. For 10-20 km horizontal separation the phase difference between two profiles would be $360°/(50...100) \approx 4°...7°$. I doubt that the determination of vertical phases is that accurate! The use of small separations will therefore introduce a strong random component, resulting in too large phase differences on average and, hence, underestimation of horizontal wavelengths. This may also explain some of the differences between COSMIC and HIRDLS horizontal wavelengths in Fig. 10. Therefore I recommend to revise Fig. 10 using only longer horizontal separations for COSMIC. I leave it to the authors which range of horizontal separations is suitable, keeping in mind that separations should not be too long, and sufficient statistics is needed for the horizontal distributions in Fig. 10. Possible consequences of too short separations should be briefly mentioned already on p.3193. The discussion on pp.3196/7 should be adapted accordingly.

    Authors' Response: We agree with the reviewer that short horizontal separations of profile-pairs introduces a large source of error in the determination of k_h. We have added an Appendix A (with two new figures) to specifically address the validity, possible errors and subsequent bias of the methodology.

17. **p.3193, ll.22/23ff:** ***Reviewer's Comment:*** p.3193, ll.22/23ff: Horizontal separations as short as 1020km may result in unphysically short horizontal wavelengths. Are these values used for Fig. 10, or are they filtered out before?

    Authors' Response: We use horizontal wavelengths between 100-5000 km for the maps in Figure 10. We have included this information in Section 4.1, and justified the lower limit in Appendix A.

18. **p.3195, l.4:** ***Reviewer's Comment:*** An illustration of this geometry can be found in Preusse et al. (2009).

    Authors' Response: Reference included as suggested.

19. **p.3195, ll.11-13:** ***Reviewer's Comment:*** It is not clear that this estimate of momentum flux is necessarily a lower bound. Your analysis technique focuses on strong wave events, causing an increase of E_p by a factor of 3-5 in Fig. 7. This might overcompensate the low-bias in k_h and the restriction to low λ_Z values introduced by the analysis technique. Suggestion: omit the final sentence in Sect. 4.1.

    Authors' Response: Agreed, sentence omitted.

20. **p.3195, ll.20/21:** ***Reviewer's Comment:*** Theoretically, COSMIC and HIRDLS should be sensitive to about the same part of the gravity wave spectrum (Preusse et al., 2008, Sect. 5).

    Authors' Response: There are subtle differences in the useful stratospheric vertical height windows, but generally agreed. Changed "different but overlapping" to "overlapping".

21. **p.3196, ll.16ff:** ***Reviewer's Comment:*** p.3196, ll.16ff: Possibly, differences in the geographical distribution of λ_H are caused by the short horizontal separations used for COSMIC. This should be checked. See also specific comments 16 and 17.

    Authors' Response: This was checked during the analysis, and has been checked again. We could find no link between the geographical distribution of COSMIC λ_H and horizontal separation, Δr despite a link being present in absolute terms as discussed in Appendix A. It is likely therefore that the error in λ_H estimation exceeds any geographical structure.

22. **p.3197, l.8:** ***Reviewer's Comment:*** p.3197, l.8: "slightly lower" to "considerably lower" (the horizontal wavelength scale differs by about a factor of two!)

    Authors' Response: Agreed, changed.

23. **p.3197, l.25:** ***Reviewer's Comment:*** This is not an effect inherent in the HIRDLS observations. HIRDLS and GPS-RO observational filters should be similar. Suggestion: "since HIRDLS generally resolves" to "since our HIRDLS analysis generally resolves".

    Authors' Response: Agreed. Changed as suggested.

We additionally would like to thank the reviewer for their detection of typographical errors.

Manuscript prepared for Atmos. Chem. Phys. Discuss.
with version 2014/09/16 7.15 Copernicus papers of the LaTeX class copernicus.cls.
Date: 15 May 2015

The southern stratospheric gravity-wave hot spot: individual waves and their momentum fluxes measured by COSMIC GPS-RO

N. P. Hindley[1], C. J. Wright[1], N. D. Smith[1], and N. J. Mitchell[1]

[1]Centre for Space, Atmospheric and Oceanic Sciences, University Of Bath, BA2 7AY, UK

Correspondence to: Neil Hindley (n.hindley@bath.ac.uk)

Abstract

~~During austral winter the mountains of the southern Andes and Antarctic Peninsula are a known hot spot of intense gravity wave momentum flux. There also exists a long leeward region of increased gravity wave energy that sweeps eastwards from the mountains out over the Southern Ocean, the source of which has historically proved difficult to determine. In this study~~ Nearly all general circulation models significantly fail to reproduce the observed behaviour of the Southern wintertime polar vortex. It has been suggested that these biases result from an under-estimation of gravity-wave drag on the atmosphere at latitudes near 60°S, especially around the "hot-spot" of intense gravity wave fluxes above the mountainous Southern Andes and Antarctic peninsula. Here, we use Global Positioning System (GPS) Radio Occultation (RO) data from the ~~Constellation Observing System for Meteorology, Ionosphere and Climate (COSMIC)~~ COSMIC satellite constellation to ~~investigate the distribution, variability and sources of~~ determine the properties of gravity waves in the ~~hot spot region and over the Southern Ocean. We present evidence that suggests a southward focusing of waves into the stratospheric jet from sources to the north. We also describe a~~ hot-spot and beyond. We show considerable southward propagation to latitudes near 60°S of waves apparently generated by the southern Andes. We propose that this propagation may account for much of the wave drag missing from the models. Furthermore, there is a long leeward region of increased gravity-wave energy that sweeps eastwards from the mountains over the Southern Ocean. Despite its striking nature, the source of this region has historically proved difficult to determine. Our observations suggest that this region includes both waves generated locally and orographic waves advected downwind from the hot-spot. We describe and use a new wavelet analysis technique for the quantitative identification of individual waves from COSMIC temperature profiles. This analysis reveals different geographical regimes of wave amplitude and short-timescale variability in the wave field over the Southern Ocean. Finally, we ~~take advantage of~~ use the large numbers of closely spaced pairs of profiles from the deployment phase of the COSMIC constellation in 2006 to make estimates of ~~gravity wave~~ gravity-wave horizontal wavelengths. We show that, given sufficient

numbers of these pairsobservations, GPS-RO can then produce physically reasonable estimates of stratospheric gravity wave momentum flux in the hot spot region that hot-spot, which are consistent with other studies. The results are discussed measurements made by other techniques. We discuss our results in the context of previous satellite and modelling studies to build up a better picture develop a better understanding of the nature and origins of waves in the southern winter stratosphere. stratosphere.

1 Introduction

Gravity waves are propagating mesoscale disturbances that transport energy and momentum in fluid environments. They are a vital component of the atmospheric system and a key driving mechanism in the middle and lower atmosphere through drag and diffusion processes (e.g. Fritts and Alexander, 2003, and citations therein). However, despite their importance, considerable uncertainty remains about gravity-wave sources, fluxes, propagation and variability.

A striking example of the importance of accurately assessing gravity-wave fluxes is that that nearly all global climate models (GCMs) have a systematic bias in their representation of the southern stratosphere. In particular, in the models the break down of the winter polar vortex occurs too late in the year, the polar vortex winds are too strong and the polar vortex temperatures are too low. This “cold-pole” bias is a long-standing problem and has been identified as a serious impediment to model progress, leading to discrepancies in properties including simulated Antarctic ozone trends and southern-hemisphere climate (e.g. McLandress et al., 2012) . These problems are believed to arise because the models are deficient in gravity-wave drag in the stratosphere at latitudes near 60S. This deficiency may arise because in the real atmosphere waves from other latitudes propagate into this latitude belt, or because the sources of gravity waves in the models under-represent the in situ generation of waves. Determining the nature of gravity waves at latitudes near 60S is thus a significant problem.

During austral winter, observations have revealed the southern hemisphere stratosphere ~~is~~ to be home to some of the most intense gravity wave activity on Earth. At ~~southern high-latitudes~~high southern latitudes, the mountains of the southern Andes and Antarctic Peninsula are a hot spot of stratospheric gravity wave momentum flux ~~(e.g. Ern et al., 2004; Alexar~~ Several second-order hot spots include South Georgia (Alexander et al., 2009) and other small islands in and around the Southern Ocean (Alexander and Grimsdell, 2013; Hoffmann et al., 2013).

Accompanying the momentum flux hot spot is a long leeward distribution of increased gravity wave energy stretching eastwards from the southern Andes, Drake Passage and Antarctic Peninsula far over the Southern Ocean. This feature has puzzled researchers since it was first seen in spaceborne observations. Despite more than a decade of close observation (e.g. Wu and Waters, 1996; Wu and Jiang, 2002; Ern et al., 2004; Hei et al., 2008; Alexander et al., 2008, 2009; Yan et al., 2010; Gong et al., 2012; Hendricks et al., 2014; Preusse et al., 2014) its origins are still not incontestably understood.

It has been suggested that gravity waves in this region may have a number of orographic and non-orographic sources, such as the leeward propagation of mountain waves from the southern tip of South America and/or the northern tip of the Antarctic Peninsula (Preusse et al., 2002; Sato et al., 2009, 2012), baroclinic instabilities from tropospheric storm systems (Hendricks et al., 2014; Preusse et al., 2014) or spontaneous adjustment arising independently from, or as a result of, either or both of these primary processes. It is likely that the gravity waves observed in this region are a result of some or all of these processes overlapping in spatial and temporal regions.

However, quantitatively identifying and describing the location, magnitude and short-timescale variability of each gravity wave source through close observation has proved exceptionally challenging. It is perhaps for this reason that the current generation of General Circulation Models (GCMs) exhibit strong disagreement in the magnitude and distribution of the flux of horizontal ~~psuedo-momentum (henceforth~~ psuedomomentum (hereafter referred to as momentum flux) due to gravity waves in the southern hemisphere stratosphere during austral winter compared to observations (Geller et al., 2013). Particularly large dis-

crepancies are found over the mountains of the southern Andes and Antarctic Peninsula suggesting even orographic wave drag is not simulated consistently.

For the majority of operational GCMs used in numerical weather prediction (NWP), many gravity waves are sub-gridscale phenomena and their effects must be parametrized. Parametrizations vary greatly between GCMs, but tuning parameters may for example be chosen in order to produce comparable monthly-mean zonal-mean wind fields to observations (Geller et al., 2013) or obtain a realistic quasi-biennial oscillation (QBO) (e.g. Scaife et al., 2000) while remaining physically plausible. However, a current scarcity of robust observations of key gravity wave parameters means that these parametrizations are poorly constrained (Alexander et al., 2010). With the advent of increased computing power in recent years, high spatial resolution GCMs without the need for gravity-wave parametrizations are becoming available (e.g. Watanabe et al., 2008). Such high-resolution modelling studies are promising (e.g. Sato et al., 2012), but discrepancies between observed and modelled parameters still remain. An in-depth review of the current state of gravity-wave modelling is presented by Preusse et al. (2014).

~~In the present study,~~ All of the above factors highlight the need for accurate measurements of gravity-wave sources, energies, fluxes and variability. Here, we use Global Positioning System radio occultation (GPS-RO) data to investigate the nature and origins of waves in the southern stratospheric gravity wave hot spot and associated leeward distribution of enhanced gravity wave energy. In Section 2, we present maps and cross-sections of gravity wave energy in the southern hemisphere, with implications for oblique focussing and leeward propagation of gravity waves into the southern stratospheric jet. In Section 3, we ~~present a~~ propose a new method for the quantitative identification of individual waves from GPS-RO profiles. We use this method to investigate the geographical distribution of wave amplitudes and short-timescale variability of individual gravity waves in the wave field over the Southern Ocean. In Section 4, we present a method for the estimation of gravity wave momentum flux from GPS-RO measurements over the southern Andes and Antarctic Peninsula using pairs of closely spaced and closely timed profiles. Our results are discussed in

the context of other studies in Section 5, and in Section 6 the key results of the present study are summarised.

1.1 COSMIC GPS Radio Occultation

Launched in April 2006, The Constellation Observing System for Meteorology, Ionosphere and Climate (COSMIC) mission consists of six low Earth orbit ($\sim$800 km) satellites at $\sim$72° inclination and 30° separation. A detailed description of the COSMIC constellation and the radio occultation process is provided by Liou et al. (2007). Each satellite tracks occulting GPS satellites as they rise above or set below the Earth's horizon. As the GPS signal traverses the atmospheric limb, phase delay measurements attributable to changing vertical gradients of refractivity in the atmosphere are measured. Taking an integral along the line of sight, vertical profiles of dry temperature and pressure can be computed at the tangent point of the occultation via an Abel inversion (Fjeldbo et al., 1971). The dry temperature conversion breaks down in the presence of water vapour, but works well in the stratosphere, where water vapour is negligible. Kursinski et al. (1997) estimated a temperature retrieval accuracy of $\sim$0.3 K between 5-30 km, while Tsuda et al. (2011) verified multiple profiles with nearby radiosonde flights, returning discrepancies typically less than 0.5 K between 5-30 km.

In the present study we use COSMIC level 2 (version 2010.2640) post-processed dry temperature data from launch in April 2006 to the end of 2012. The sampling density of the COSMIC constellation in its final deployment configuration for a typical month in the southern hemisphere is shown in Figure 1. Good coverage at high latitudes and a band of preferential sampling at around 50°S as a result of orbital geometry means that COSMIC GPS-RO is well suited to a study of the southern gravity wave hot spot and the surrounding area.

1.1.1 Vertical and horizontal resolution limits

Currently, no single observational technique can study the entire gravity wave spectrum. Each technique is sensitive to a specific portion of the gravity wave spectrum, referred to as its observational filter (Alexander and Barnet, 2007; Preusse et al., 2008; Alexander et al., 2010).

The expected vertical and horizontal resolutions of GPS-RO are discussed at length by Kursinski et al. (1997). They showed that in the stratosphere, where reasonable spherical symmetry of the local atmosphere can be assumed, the vertical resolution ΔZ ~~of GPS-RO~~ is primarily limited by Fresnel diffraction as

$$\Delta Z \sim\approx 2\left(\lambda L_T\right)^{\frac{1}{2}} \approx 1.4\,\text{km} \tag{1}$$

where $\lambda = 19\,\text{cm}$ is the GPS L1 wavelength and ~~$L_T \sim 28500$~~ $L_T \approx 28500\,\text{km}$ is the distance from the GPS satellite to the tangent point. ~~From these values we find $\Delta Z \sim 1.4\text{km}$.~~ The vertical resolution of GPS-RO improves significantly below the tropopause due to the exponential increase of refractivity gradient with decreasing altitude, but the combination of sharp vertical temperature gradient changes, increased humidity and smaller wave amplitudes make gravity wave study in this region difficult with GPS-RO via traditional methods.

Kursinski et al. (1997) showed that the horizontal line-of-sight resolution ΔL of GPS-RO could be defined as the horizontal distance travelled by the GPS ray as it enters and exits an atmospheric layer with vertical resolution ΔZ. By a first order geometric argument, ΔL and ΔZ are approximately related as

$$\Delta L = 2(2R\Delta Z)^{\frac{1}{2}} \tag{2}$$

where R is the radius of the atmosphere at the tangent point. The stratospheric horizontal line-of-sight resolution corresponding to a vertical resolution 1.4 km is ~~$\sim$~~$\approx$270 km. Gravity waves with $\lambda_H \lesssim 270\,\text{km}$ in the line of sight are hence ~~unlikely~~ less likely to be detected by GPS-RO. However, if the line of sight is not aligned with the wave's horizontal wavenumber

vector, the projection of λ_H in the line of sight may be longer. This means that some waves with $\lambda_H < 270$ km may be resolved. As discussed by Alexander et al. (2009), orographic waves generated by the mountains of the southern Andes and Antarctic Peninsula may tend to have roughly westward orientated horizontal wavenumber vectors, and the majority of COSMIC occultations in this region tend to be preferentially aligned towards the north-south axis. As a result, the projection of λ_H in the COSMIC line of sight is longer and the likelihood of orographic wave detection over this region is increased.

The cross-beam horizontal resolution in the stratosphere is around 1.4 km, being only diffraction limited since horizontal refractivity gradients are generally small. This is of importance to our momentum flux study in section 4.

2 The gravity wave hot-spot and leeward region of increased E_p

In this section, we investigate the seasonal variability and distribution of potential energy per unit mass E_p in the southern hemisphere using COSMIC GPS-RO. E_p is a fundamental property of the gravity wave field and can provide a useful proxy for gravity wave activity.

In satellite observations, E_p is often derived from temperature perturbations around a background mean and can hence be calculated independently in each temperature profile. To calculate E_p, we first interpolate each dry temperature profile $T(z)$ to 100m resolution over the altitude range 0-50 km. We obtain a background temperature profile $\bar{T}(z)$ by low-pass filtering $T(z)$ with a 2nd order Savitzky-Golay filter (Savitzky and Golay, 1964) with an 18 km frame-size and compute $T(z) - \bar{T}(z)$ to yield a temperature perturbation profile $T'(z)$.

~~The choice of this~~ Features with vertical scales less than ~2 km cannot be reliably disassociated with noise in GPS-RO temperature profiles (Marquardt and Healy, 2005) , therefore we apply a 2nd order Savitzky-Golay low-pass filter ~~and subtraction method provides a dynamic cut-off that generally transmits features with $\lambda_Z \lesssim 10$~~with a 3 km ~~into our perturbation profile~~ frame size to suppress these small-scale features in $T'(z)$. ~~Transmission of vertical wavelengths longer~~ Note that this step has virtually no effect on vertical wavelengths greater

than ~~104~~ km~~decreases with increasing wavelength. A transmission function of this processing step~~ . The transmission functions for each step in our analysis is shown in ~~figure 6and discussed in more detail in section 3.1.~~ Figure 6, and discussed further in Section 3.1. For the calculation of E_p in this section, only the blue and green dashed lines in Figure 6 apply.

This analysis provides a dynamic cut-off for vertical features in $T'(z)$. Features with vertical scales $\sim 3-14$ km are generally transmitted with a factor of at least 0.5, however transmission of vertical wavelengths longer than ~ 13 km (shorter than 4 km) decreases with increasing (decreasing) wavelength. It is important to note that no digital filter can provide a perfect cut-off in the frequency domain without introducing ringing artifacts into the spatial domain via the Gibbs phenomenon. We select the Savitzky-Golay filter as a reasonable trade-off between Gibbs ringing in the spatial domain and a sharp transition into the frequency stop band.

We ~~then~~ use $T'(z)$ and $\bar{T}(z)$ to compute $E_p(z)$ as

$$E_p(z) = \frac{1}{2}\left(\frac{g}{N}\right)^2 \left(\frac{T'(z)}{\bar{T}(z)}\right)^2 \tag{3}$$

where g is acceleration due to gravity and N is the local Brunt-Väisälä frequency. It is not meaningful to take E_p at a single height z from a single profile since a full wave cycle does not exist (Alexander et al., 2008). Hence, E_p is often taken as an integral over a specified height interval when used as a proxy for gravity wave activity (e.g. Hei et al., 2008).

Unlike previous studies such as Alexander et al. (2009), no planetary wave removal techniques are applied to these data. At high latitudes, planetary waves typically have vertical scales much longer than 10 km, hence they are generally removed by our filtering method. ~~Furthermore, the long leeward distribution of enhanced gravity wave activity that we expect to see over the southern Atlantic and Indian Oceans from other studies appears morphologically similar to an $s = 1$ or part of an $s = 2$ planetary wave and may be suppressed by a Fourier or wavelet transform-based removal technique.~~ We recognise however that some low-level planetary wave features may remain in the post-processed data.

2.1 Geographic distribution of E_p in the southern hemisphere

Figure 2 shows E_p in the southern hemisphere for each month in 2010 over the height interval 26-36 km. ~~This~~ Note that this 10 km averaging window generally undersamples waves with $\lambda_Z > 10$ km~~, which further decreases the likelihood of observing planetary wave artifacts in the data~~.

We observe increased levels of E_p in austral winter and lower values in austral summer, consistent with other GPS-RO studies (e.g. Hei et al., 2008; Alexander et al., 2009). Between June and November, we see in Figure 2 a long leeward region of increased E_p stretching clockwise from the Southern Andes, Drake Passage and Antarctic Peninsula at around 70°W to around 180°E. This long leeward region of increased E_p is consistent with studies using other limb sounders such as the Upper Atmosphere Research Satellite Microwave Limb Sounder (UARS-MLS) (e.g. Wu and Waters, 1996), Cryogenic Infrared Spectrometers and Telescopes for the Atmosphere (CRISTA) (e.g. Ern et al., 2004) and the HIgh Resolution Dynamics Limb Sounder (HIRDLS) (e.g. Yan et al., 2010).

The magnitude and distribution of E_p in Figure 2 is also consistent with results from a high-resolution modelling study by Sato et al. (2012) using the T213L256 "Kanto" GCM developed by Watanabe et al. (2008). This is significant since Sato et al. used no gravity wave parametrizations, such that all resolved waves effects were spontaneously generated. They showed a long leeward distribution of E_p at 10 hPa (~31 km) stretching clockwise around the southern ocean from the southern Andes and Antarctic Peninsula to around 180°W during June-October. They proposed a downwind propagation mechanism for orographic waves from the mountains of the southern Andes and Antarctic Peninsula, whereby a wave could be freely advected by the component of the mean wind perpendicular to the ~~the~~ wave's horizontal wavenumber vector, and primarily attributed the long leeward distribution to this mechanism.

Some differences in our observed distribution of gravity wave E_p are apparent, however. ~~Sato et al. (their Figure 2)~~ Sato et al. (2012, their Figure 2) showed maximum E_p directly over the mountains of the southern Andes at 10 hPa. ~~Using data from the Atmospheric~~

~~Infrared Sounder (AIRS) instrument aboard NASA's Aqua satellite, Hendricks et al. (2014) also observed peak values directly~~ Likewise, Yan et al. (2010, their Figure 5) revealed similar distributions of mean gravity wave amplitude T' from HIRDLS data that also maximised over the mountains ~~in a similar pattern~~and slowly decreased eastward. In our results, we see some enhancement over the mountains in the height range 26-36 km ($\sim$22-5 hPa) in Figure 2, but maximum values are usually observed well to the east ~~. This suggests that GPS-RO is preferentially but not exclusively sensitive to the waves in the long leeward region of increased~~ over the oceans during 2010. Other years show similar distributions (omitted for brevity).

One possible explanation may relate to the range of vertical wavelengths to which our analysis method is sensitive. For mountains waves, vertical wavelengths directly over the mountains can be quite long (e.g. Alexander and Teitelbaum, 2011) . As previously discussed, our analysis method is primarily sensitive to waves with $4 \gtrsim \lambda_Z \gtrsim 13$ km, and significant amplitude underestimation occurs for waves with $\lambda_Z \gtrsim 13$ km. It could be that the contribution of these long λ_Z waves directly over the mountains to the E_p ~~out over the ocean. The observational filter of GPS-RO hence implies these waves are likely to be low-frequency inertia-gravity waves with relatively low vertical group velocities and long dwell times over the measured height range, preferentially increasing their likelihood of detection. These waves are very commonly seen in lower stratosphere observations, and can often be found far from their sources (Fritts and Alexander, 2003)~~ distributions in Figure 2 is underestimated by our analysis method.

Sato et al. (2012) also observed regions of downward energy flux. In particular they found that, in the region immediately eastward of the southern tip of South America, up to 10% of the E_p distribution consisted of downward propagating waves. This suggests that ~~a significant portion~~ some of the E_p ~~distribution in our results~~ in our observed distribution may correspond to waves that are propagating downward.

The sources of waves in the long leeward region of increased E_p are currently a topic for debate. As mentioned above, Sato et al. (2012) suggested that increased E_p over 70°W-180°E could be primarily due to mountain waves from the southern Andes and

Antarctic Peninsula that have been advected downwind, but the rest of the enhancement was likely the result of other mechanisms~~such as spontaneous adjustment~~. Other studies ~~however~~ suggest that much of the enhancement is primarily the result of non-orographic wave sources in and around the Southern Ocean (e.g. Hendricks et al., 2014; Preusse et al., 2014). Furthermore, the distribution of increased E_p in Figure 2 is very reminiscent of southern hemisphere storm tracks (Hoskins and Hodges, 2005) . It is thus likely that the observed distribution of E_p is the result of a number of orographic and non-orographic processes, each playing different roles in different geographical regions. In the next section we use an extended altitude range to build vertical cross-sections of stratospheric E_p in the long leeward distribution to investigate this further.

2.1.1 ~~Vertical distribution of E_p over the southern Andes and Antarctic Peninsula~~

2.2 Vertical distribution of E_p over the southern Andes and Antarctic Peninsula

An interesting result discussed by Sato et al. (2009) and presented in Sato et al. (2012) was the apparent focusing of gravity waves into the southern stratospheric jet in the Kanto GCM. In a meridional cross-section from 30°S-70°S centred on 55°W (their figure 13), Sato et al. showed increased E_p values in a distinct slanted vertical column over the southern Andes during 5 days in August. Energy flux vectors showed a large flow of energy ∼1500-2000 km southward over the height region 100 hPa (∼16 km) to 1 hPa (∼48 km). The flow appeared to focus towards the centre of the jet, where mean zonal winds were strongest.

In our Figure 3, we select a thin meridional cross-section of normalised monthly-mean COSMIC E_p for August 2010 centred on 65°W. This is close to the cross-section used by Sato et al. (2012). Since ~~gravity wave amplitudes often increase with height~~raw E_p is expected to increase with increasing altitude and decreasing pressure, each height level in Figure 3 has been normalised ~~in order to highlight the~~ such that the lowest value is equal to 0 and the highest value is equal to 1 (Wright and Gille, 2011) . This approach highlights the vertical structure. Although temperature profiles from COSMIC typically exhibit increased noise above around 40 km, ~~this~~ the normalisation and the increased number of measure-

ments in the month-long time window potentially allow us to resolve large persistent features at higher altitudes, albeit with caution.

A slanted vertical column of increased E_p in the height region 22-35 km and a near vertical column from 35-50 km is evident in Figure 3. The lower section of the column traverses nearly 1500 km southward over the height region 22-35 km. This suggests a clear focusing effect similar to the one suggested by Sato et al., although we cannot recover energy flux information from COSMIC. A monthly-mean zonal wind field $\bar{U}$ (thick contours) from ECMWF operational analysis is used in Figure 3 to show the approximate position of the southern stratospheric jet over the southern Andes and Antarctic Peninsula during August 2010. The gradient of ~~this southward slant~~ the southward slant in E_p is greatest when the horizontal gradient in zonal wind ~~strength~~ speed is greatest, such that waves appear to be focused into the centre of the stratospheric jet. This observation is consistent with meridional ray-tracing analyses in the Kanto model (Watanabe et al., 2008; Sato et al., 2009, 2012). Above ~35 km ~~however,~~ the horizontal gradient in zonal mean wind ~~strength~~ speed is low and waves appear to generally propagate upward without further latitudinal drift.

This result suggests that waves observed at around 30-40 km over the southern tip of South America and the Drake Passage may have sources further north. In a ray-tracing analysis for an idealized background zonal wind field, Sato et al. (2012, their Figure 5) showed that zero ground-based phase velocity waves with $\lambda_H = 300$ km launched from the southern Andes could propagate eastward and southward by up to around 2500 km and 1000 km respectively ~~in an idealized background zonal wind field~~before reaching an altitude of 40 km. They found that waves launched from north of 45°S did not propagate upward due the mean wind being too weak. Our results suggest that such waves may indeed propagate from sources north of 45°S, since the slanted column in Figure 3 is observed all the way down to 22 km over 30-45°S . This could imply that there are significant time periods where the tropospheric zonal winds are strong enough to allow vertical propagation of mountain waves from these sources.

An important consideration of this work is the effect of the range of gravity wave vertical wavelengths to which our observations and analysis are limited. For mountain waves

$$\lambda_Z \approx \frac{2\pi U_{||}}{N} \tag{4}$$

where $U_{||}$ is the component of mean wind speed $\bar{U}$ parallel to the wave's horizontal wavenumber vector and N is the local Brunt-Väisälä frequency (Eckermann and Preusse, 1999). Our analysis is primarily sensitive to waves with $4 \gtrsim \lambda_Z \gtrsim 13$. From Equation 4, mountain waves could have vertical wavelengths too long to be detected for $U_{||} \gtrsim 40 - 50\,\mathrm{ms}^{-1}$. However, horizontal wavenumber vectors of mountain waves over the southern tip of South America have been shown to rotate southwards poleward of 45°S over the Drake Passage (e.g. Alexander and Teitelbaum, 2011) . Here, the mean wind vector $\bar{U}$ and the horizontal wavenumber vector are no longer parallel and shorter vertical wavelengths are not precluded since $U_{||}$ is reduced. Therefore the slanted vertical column of E_p in Figure 3 could be due to mountain waves and could suggest meridional propagation.

Sato et al. also suggested that a symmetric northward focusing effect may occur for orographic waves from the Antarctic Peninsula. We investigated ~~this~~ such an effect using COSMIC data~~(not shown) and although a very~~ . Though a slight suggestion of ~~this effect~~ northward meridional focussing may be evident (not shown), we could ~~find no such clear behaviour~~ not find an effect so clear as is observed over the southern Andes.

2.2.1 ~~Vertical distribution of E_p over the Southern Ocean~~

2.3 Vertical distribution of E_p over the Southern Ocean

We also investigate the vertical distribution of wave energies over the Southern Ocean. Figure 4 shows ~~normalised~~ altitude-normalised E_p in a zonal cross-section ~~centred on 50°~~from $40 - 60$°S during August 2010. As in Figure 3, E_p is normalised at each height level in order to highlight the vertical structure.

The vertical column of increased E_p located around 70°W in Figure 4 is the projection in the zonal domain of the vertical column evident in Figure 3. This column is highly suggestive of intense localised mountain wave activity from the southern Andes. The relative intensity of this column at lower altitudes suggests that, within the observational filter of ~~COSMIC~~our COSMIC analysis, the southern Andes is the dominant source of orographic wave activity in this latitude band. If small mountainous islands in the Southern Ocean are also significant orographic sources, as has been suggested in recent studies (Alexander et al., 2009; McLandress et al., 2012; Alexander and Grimsdell, 2013), then it is likely that waves from these islands either (1) fall outside the observation filter of ~~GPS-RO~~our analysis; (2) have small amplitudes; or (3) are too intermittent over monthly time-scales to be revealed in our analysis.

The column at 70°W appears to persist over the full height range in Figure 4. However, between 25-35 km the largest values are observed well eastward, between 60°E-60°W. These peaks are located in a deep region of increased E_p between 20-40 km and 30°W-90°E, which is the projection in the vertical domain of the long leeward region of increased E_p seen in Figure 2.

At first glance, Figure 4 suggests that this long leeward region of increased E_p is strongly associated with mountain waves from the southern Andes and Antarctic Peninsula region. The lack of significant gravity wave energies upwind (westward) of the mountains and the intensity of energies downwind (eastward) is clear. ~~As suggested by Sato et al. (2012) , the~~ Sato et al. (2012) suggested that the leeward distribution of increased E_p ~~may~~ might be the result of primary mountain waves from the southern Andes and Antarctic Peninsula that have been advected downwind. However, Sato et al. also showed that waves with λ_H<350 km rarely travelled further east than the prime meridian via this mechanism, even under ideal conditions. This suggests that ~~it is orographic waves with $\lambda_H \gtrsim$350km that~~ if downwind-advected orographic waves do contribute to the region of increased E_p eastwards of the prime meridian~~via this advection mechanism.~~

~~It is also possible that primary~~ , they likely have $\lambda_H \gtrsim$350 km. Primary orographic waves from the southern Andes and Antarctic Peninsula may ~~contribute to the long leeward region~~

of increased E_p then also contribute through secondary mechanisms, such as the local generation of waves in and around the stratospheric jet through breaking or other wave-mean flow interaction. The absence of significantly increased energy downwind of the Andes below 20km interactions (Bacmeister and Schoeberl, 1989) . Waves generated by in-situ instabilities and spontaneous adjustment around the stratospheric may also play a part.

Hoskins and Hodges (2005) presented a detailed view of southern hemisphere storm tracks in ECMWF Re-Analysis (ERA-40) data. During austral winter, storms generally tended to maximise over the southern Atlantic and Indian sectors, spiralling poleward and eastward over the Pacific sector. Such storm-tracks may indicate intense sources of non-orographic wave activity. O'Sullivan and Dunkerton (1995) showed that non-orographic waves generated around the tropospheric jet can have vertical wavelengths of a few kilometres. These wavelengths may be too short to be resolved by COSMIC. Mean zonal wind generally increases with height as seen in Figure 4indeed suggests that many of the waves present in this long leeward region of increased E_p above 20km between 40-60°S may have been generated locally. . This may refract these waves to longer vertical wavelengths such that they become visible to COSMIC. This could explain the relative reduction of wave activity at low altitudes over 30°W to 120°E in Figure 4. The spiralling effect of the storm-tracks might also mean that these intense sources of non-orographic waves may begin to move poleward out of the latitude band used in Figure 4. This may explain the relative decrease in intensity further eastward.

We suspect therefore that the leeward region of increased E_p over 70°W-60W-90°E in Figure 4 is likely dominated by (1) primary orographic waves with λ_H>350$\lambda_H > 350$ km from the southern Andes or Antarctic Peninsula that have been advected downwind; and (2) and secondary waves with non-zero phase speeds generated in the breaking zones of these primary orographic waves(Bacmeister and Schoeberl, 1989) . These results do not however ; and (3) non-orographic wave activity associated with storm tracks over the oceanic sectors. Note that due to vertical resolution limitations, these results may underestimate the contribution of (3). They also do not preclude the existence of other non-orographic sources in the re-

gion ~~, as will be discussed in Section 5~~such as jet instabilities or spontaneous adjustment mechanisms.

3 Individual waves

The long leeward region of increased E_p observed over the southern Atlantic and Indian Oceans is a persistent feature each year during austral winter, though some interannual variability exists. Multiple year averages are one way to learn about dominant processes in a region, but in order to investigate properties of a specific wave field, such as vertical wavelength or wave amplitude, a key question must first be answered: is a wave present? Once this has been answered, it becomes possible to investigate the distribution and species of individual gravity waves in a geographical region.

3.1 Wave identification (Wave-ID) methodology

This section describes ~~the processing chain~~ our methodology for identifying individual gravity waves from COSMIC GPS-RO temperature profiles~~, which is illustrated~~. The method is illustrated for an example profile in Figure 5.

We begin by extracting temperature perturbations $T'(z)$ from each profile (Figure 5a) as described in Section 2. ~~Features with vertical scales less than ~2km cannot be reliably disassociated with noise in GPS-RO temperature profiles (Marquardt and Healy, 2005). Hence, as a noise-reduction step, we apply a 2nd order Savitzky-Golay low-pass filter with a 3km frame size to suppress these small-scale features. Note that this step has virtually no effect on vertical wavelengths greater than ~4km. The transmission function of each step in this analysis is shown in Figure 6.~~

~~Next we~~ We then window the profile with a Gaussian of Full Width at Half Maximum (FWHM) 22 km centred at a height of 30 km (Figure 5b). The purpose of this step is to focus on the height range of the profile most appropriate for gravity wave study using COSMIC GPS-RO data. This height range is chosen to generally correspond to the largest vertical region where (1) the error in bending angle is low; (2) we are unlikely to encounter spu-

rious temperature perturbation anomalies due to incomplete background removal around the tropopause; and (3) retrieval errors associated with ionospheric effects are low (see Tsuda et al., 2011). This corresponds to a region typically between 20-40 km. The choice of a Gaussian window minimises edge effects that may arise in subsequent spectral analysis. ~~We then normalise this~~

We normalise the windowed profile such that the root-sum-square (RSS) " energy" of the profile is equal to 1 (Figure 5c).

~~Next, we~~ Note that the term "energy" is defined as the sum-square of the values of the windowed profile and does not take any other physical meaning here. We then set the average of the profile to zero, and compute the Continuous Wavelet Transform (CWT) of the ~~normalised profile. To retain phase information, we use~~ windowed, normalised and zero-averaged profile. For scale parameter a and position along the profile b, the spectral coefficients $C(a,b)$ of the CWT are given as

$$C(a,b) = \frac{1}{\sqrt{a}} \int_{-\infty}^{\infty} T'(z)\psi^* \left(\frac{z-b}{a} \right) dz \tag{5}$$

where $T'(z)$ is our normalised, windowed and zero-averaged perturbation profile and ψ^* is the complex conjugate of the analysing wavelet. We choose an 8th order complex Gaussian wavelet for ~~the transform. Figure 5d shows squared absolute spectral amplitude of the cospectrum $|C_{(z,\lambda_Z)}|^2\psi$~~, such that phase information is retained. For such a Gaussian wavelet, scale parameter a, which corresponds to a "stretching" of the wavelet, is approximately related to wavelength λ by

$$\lambda \approx \frac{a\Delta z}{f_{cent}} \tag{6}$$

where Δz is sampling interval and f_{cent} is the dominant central frequency of the wavelet for scale parameter $a = 1$ and unit integer interval spacing ($\Delta z = 1$). Position along the profile b corresponds to altitude z at intervals of Δz.

We are thus able to describe the spectral coefficients $C(a, b)$ in terms of vertical wavelength λ_Z and altitude z. The absolute magnitudes of the spectral coefficients $|C(\lambda_Z, z)|$ are plotted in Figure 5d.

As a result of the normalisation ~~, the~~ and zero-averaging, the absolute magnitudes of these coefficients can be interpreted as coefficients of ~~$|C_{(z,\lambda_Z)}|^2$ in Figure 5d can be assigned a more physical meaning. Each value represents the fractional "energy" of the profile "captured" by each wavelet at each height. Note that the term "energy" is defined as the sum-square of the values of the windowed perturbation profile and does not take any other physical meaning here. The squared absolute spectral amplitude $|C(z, \lambda_Z)|^2$ is hence a confidence metric as a function of z~~ pseudo-correlation, describing the correlation between the profile and a wavelet of wavelength λ_Z ~~that represents how wave-like the transformed profile was at each height~~ at altitude z~~for each vertical wavelength λ_Z. High~~ . Ranging between 0 and 1, high (low) values of ~~this confidence metric~~ $|C(\lambda_Z, z)|$ imply the presence (absence) of a clear wave-like ~~features in the windowed profile. We record the maximum squared absolute spectral amplitude $C_{\text{max}} = \max\left(|C(z, \lambda_Z)|^2\right)$ located at the spectral peak~~ feature in the profile.

If the profile and the analysing wavelet are both real, both have RSS " energy" equal to 1 and are both zero-averaged, then the coefficients of the CWT can be exactly interpreted as coefficients of correlation is the usual sense. The coefficients in our analysis are strictly pseudo-coefficients of correlation, due to our choice of a complex wavelet. This choice has the advantage of producing one single peak per wave-like feature in Figure 5d, which is easier to interpret than a series of peaks corresponding to correlation/anti-correlation which would result from a non-complex wavelet.

To positively identify a wave in the profile, we require that ~~C_{max} exceeds a threshold value of 0.36~~the absolute magnitude of the spectral peak coefficient $C_{\text{max}} = \max(|C(\lambda_Z, z)|)$ is greater than or equal to 0.6. This choice is somewhat arbitrary, but it ~~roughly corresponds~~

~~to a wavelet "capturing" at least 60of the root-sum-squared "energy" of the profile~~ can be interpreted as a requirement that the profile is pseudo-correlated with a wavelet of wavelength λ_Z at position z with coefficient greater than 0.6. If this condition is satisfied, the identification is positive and we record the vertical wavelength λ_{peak} and altitude z_{peak} at C_{max}. As a result of the Gaussian windowing, z_{peak} is almost always located within one wavelength λ_{peak} of 30 km altitude, hence it is reasonable to consider this analysis method as sensitive to gravity waves at a height of around 30 km.

C_{max} can thus be regarded as a confidence metric for the existence of wave-like features in COSMIC perturbation profile. In the example in ~~figure~~ Figure 5d, ~~$C_{\text{max}} \sim 0.41$~~ the absolute spectral peak $C_{\text{max}} \approx 0.64$ such that a wave with ~~$\lambda_Z \sim 7$~~$\lambda_Z \approx 7.1$ km is positively identified at an altitude near 30 km. ~~Direct information~~ Information regarding the wave's amplitude T' ~~is lost as a result of~~ cannot strictly be obtained from the CWT, so in order to obtain an estimate of T' we find the maximum amplitude of the temperature perturbation profile $T'(z)$ over the height region $z_{\text{peak}} \pm \lambda_{\text{peak}}/2$. In the example in Figure 5b, ~~$T' \sim 2.3$~~$T' \approx 2.3$ K.

To summarise our requirements for a positive wave identification, we require that the wave (1) has an amplitude 1 K < T' < 10 K; (2) has a vertical wavelength 2 km < ~~λ_z~~ λ_{peak} < 20 km; (3) is located such that 20 km < z_{peak} < 40 km; and (4) has a confidence metric ~~$C_{\text{max}} > 0.36$~~ $C_{\text{max}} \geqslant 0.6$ as described above.

Using these criteria, we find that ~~around 25-40~~on global year-long average around 20-40% of profiles contain an indentifiable gravity wave signal~~, depending on location and season~~. In some regions and seasons, as will be seen later, this fraction can be as high as $\sim 80\%$. This wave identification method will be henceforth described as the Wave-ID method for convenience. Note that we currently limit this Wave-ID methodology to one (the dominant) wave per profile.

We note that this method preferentially selects profiles that contain a single large amplitude monochromatic wave with low levels of disassociated noise. A superposition of two waves of equal amplitude may result in neither being identified due to the confidence metric described above. This may also affect our amplitude estimation. However ~~, due to phase ambiguity~~ on average it is equally likely that the amplitude will increase or decrease as a

result of any superposition. Hence if a sufficient number of profiles are measured, this effect should average out. Wright and Gille (2013) showed that in the southern hemisphere during austral winter, and particularly in the vicinity of the southern Andes and Antarctic Peninsula, there were typically fewer overlapping waves than any other geographical region. Hence, wave identification problems associated with wave superposition are likely minimised in our geographical region of interest.

The choices we have made in our Wave-ID processing will also affect the range of vertical wavelengths we detect. Figure 6 shows transmission curves as a function of wavelength for each processing step in the Wave-ID method. As shown by the net transmission curve (black solid) in Figure 6, the combined analysis method is generally sensitive to gravity waves with 4 km < λ_z < ~~12~~13 km, with a sharp cut-off below 4 km and a more gradual cut-off above ~~12~~13 km.

The histogram in figure 6 shows vertical wavelengths of gravity waves identified by this method in the region 35-75°S and 0-90°W during June-August 2006-2012. The distribution of observed vertical wavelengths generally follows the net transmission curve of synthetic waves, with peak observations at 7 km < λ < 9 km.

A primary limitation of the Wave-ID method is the limited vertical window, which limits maximum resolvable vertical wavelength. This is due to the limited vertical extent of the high-accuracy temperature retrieval of COSMIC GPS-RO. Extending the region upwards would reduce confidence in any resolved waves due to increased noise in measurements above z ~~~≈ 38 km (Tsuda et al., 2011). If we extend the region down much further, sharp gradients in temperature around the tropopause risk introducing spurious artifacts via traditional filtering methods (Alexander and de la Torre, 2011). Furthermore, decreasing wave amplitudes with increasing pressure in addition to the presence of water vapour makes gravity wave study below the tropopause difficult via GPS-RO. We also implicitly assume that λ_Z does not change much with altitude, which might not hold true for the real atmosphere. This could decrease the probability that we will identify waves with longer λ_Z, which may help to explain the slight mis-match between the histogram in Figure 6 and the range of permitted wavelengths (solid black curve) for longer λ_Z waves.

Future work may involve (1) optimising this vertical window so as to resolve the maximum possible range of vertical wavelengths; (2) investigating the optimum threshold value above which to consider a wave identification as positive; and (3) employing methods to identify overlapping waves as described by ~~(Wright and Gille, 2013)~~ Wright and Gille (2013) .

3.2 Wave identification results

In Figure 7a we present a multi-year composite plot of E_p for June-August 2006-2012 at 30 km over the southern hemisphere. In this analysis, we take the mean E_p from all available profiles, including those where no significant waves are present. In Figure 7b we produce another composite plot of E_p but calculated using only waves identified via the Wave-ID method described above. In other words, Figure 7a is a time-averaged climatology of E_p in the region whereas Figure 7b is the mean E_p of ~~the waves themselves~~individual waves detected using the Wave-ID method during this period.

An initial observation is that much higher E_p values are apparent in Figure 7b than in Figure 7a. This is expected, since mean E_p values in Figure 7b are skewed by the exclusion of profiles ~~that did not contain a wave~~for which no wave-like feature was detected.

The same long leeward region of increased E_p sweeping around Antarctica is present in both panels of Figure 7. The largest values in both panels are generally observed just east of the southern tip of South America and the Antarctic Peninsula, decreasing eastward and reaching a minimum just west of the Drake Passage. ~~However, the Wave-ID method used~~ By comparison of the two maps from the two different methods in Figure 7~~b reveals a number of differences. Firstly, the~~ , information about wave intermittency can be inferred. The peak of the distribution of E_p in Figure 7b resides much closer to the mountains of the southern Andes and Antarctic Peninsula, but the rest of the distribution remains broadly co-located with the results in Figure 7a. The westward shift of ~~this~~ the peak implies that waves close to the southern Andes and Antarctic Peninsula have ~~large~~ on average larger amplitudes, but ~~they~~ are more intermittent ~~,~~ since this peak is diminished in the average of all available profiles. ~~Furthermore, this peak shifts westward but the~~ The rest of the distribution may therefore be less intermittent, since it remains broadly co-located ~~with the results in~~

~~Figure 7a, which suggests that the region immediately east of the southern Andes and Antarctic Peninsula is more intermittent than the rest of the distribution~~in both panels. This is consistent with the hypothesis that ~~this region~~ the region immediately east of the mountains is dominated by waves from orographic sources, which have been shown to be generally more intermittent ~~that~~ than non-orographic sources in this region (Hertzog et al., 2008, 2012; Plougonven et al., 2013; Wright et al., 2013). A small enhancement is also evident at around 160°E 65°S that may be suggestive of a contribution from orographic waves from the Transantarctic Mountains.

To further investigate the nature of the wave field in this long leeward region of increased E_p, we divide the latitude band 40-65°S into six longitudinal sectors A-F, and examine the population of waves in each sector. Sector C contains the mountains of southern Andes, Antarctic Peninsula and South Georgia. Sector B is oceanic and upwind (westward) of these mountains. Sector D is also oceanic but immediately downwind (eastward) of the mountains. Sectors A, E and F are predominantly oceanic. Figure 9 presents histograms of individual wave amplitudes identified using the Wave-ID method in each of these six sectors during June-August 2006-2012. Note that these waves are ~~the same~~ from the same profiles used to produce the E_p distribution in Figure 7b.

At first glance, the histograms of wave amplitudes in each sector in Figure 9 appear broadly similar. Approximately 20000 waves are identified in each sector and the modal amplitude is between 2-3 K. Upon closer inspection however, some important differences become apparent.

Despite containing around 4.5% and 12% fewer profiles than Sector B respectively, Sectors C and D contain around 13% and 6% more identified waves respectively. This indicates that the sectors containing and immediately downwind of the southern Andes and Antarctic Peninsula (C,D) contain significantly more identifiable waves than sectors immediately upwind. Furthermore, Sector B has the highest number of available profiles, yet the lowest number of identified waves of any sector.

We next investigate the relative distribution of wave amplitudes in each sector compared to the zonal mean to highlight any longitudinal variation in wave amplitude populations. The

rightmost panel in Figure 9 shows the difference between the histogram in each sector and the zonal mean histogram of wave amplitudes. The curves in this panel indicate that the sectors containing and downwind of the southern Andes and Antarctic Peninsula (C,D) contain significantly more large amplitude ($3 < T' < 8$ K) waves and fewer small amplitude waves ($T' < 2.5$ K) than the zonal mean, whereas upwind Sectors A, B and F contain fewer large amplitude waves and more small amplitude waves.

Three interesting conclusions are indicated by this analysis. Firstly, the geographical region downwind (eastward) of the mountains of the southern Andes and Antarctic Peninsula up to around 40°E contains significantly more identifiable gravity waves than a region of equal size upwind (westward) of the mountains.

Secondly, this downwind region contains significantly more large amplitude waves with $3 \gtrsim T' < 8$ K than the corresponding upwind region, though these large amplitude waves are still relatively rare. Since $E_p \propto (T')^2$, it is likely that the structured distribution of E_p in Figure 7b is hence the result of an increased number of large amplitude mountain waves immediately downwind of the southern Andes and Antarctic Peninsula. In a recent study involving balloon, satellite and mesoscale numerical simulations above Antarctica and the Southern Ocean, Hertzog et al. (2012) showed that rare, large amplitude waves are not only more commonly observed above mountains in this region but that these events represent the main contribution to the total stratospheric momentum flux during the winter regime of the stratospheric circulation. Hertzog et al. also showed that gravity waves populations over open ocean tend to follow a more log-normal distribution with fewer rare, large amplitude events. Our results reinforce the findings of Hertzog et al..

Thirdly, and perhaps most interestingly, differences in the number of identified waves and the relative distribution of wave amplitudes between sectors are significant, but relatively small in absolute terms. In general, each sector has strikingly similar distributions of wave amplitudes and total numbers of identified waves. This zonal uniformity in the distributions of wave amplitudes may be suggestive of strong, zonally uniform source mechanisms for gravity waves in all sectors, such as spontaneous adjustment or jet instability around the edge of the southern stratospheric jet. This is discussed further in Section 5.

4 Gravity wave momentum fluxes during JJA 2006 using COSMIC profile pairs

Gravity wave momentum flux is one of the key parameters characterising the effects of gravity waves in the atmosphere. This is of vital importance to the gravity wave modelling community, but typically difficult to obtain from observations (Fritts and Alexander, 2003; Alexander et al., 2010). Ern et al. (2004) showed that an approximation to the absolute value of momentum flux can be inferred from satellite observations of a gravity wave's amplitude T' and horizontal and vertical wavenumbers k_H and m. In the case of limb-sounding instruments such as HIRDLS and CRISTA, T' and m can be obtained directly from a single vertical temperature profile, while k_H can be estimated using the phase shift between adjacent profiles (Ern et al., 2004; Alexander et al., 2008). However, such k_H estimation methods have not routinely been applied to COSMIC, due to typically large inter-profile spacing. The scarcity of multiple profiles that are both closely spaced and closely timed with near-parallel lines of sight limits the accurate estimation of k_H in this way. Wang and Alexander (2010) investigated the use of 3 or more COSMIC profiles to make estimates of zonal and meridional horizontal wavenumbers k and l. However, as discussed by Faber et al. (2013), limitations in sampling density, aliasing and differing lines of sight restrict their approach being used in the general case.

Here we investigate an alternative approach for estimation of k_H from COSMIC GPS-RO data using a modified form of the method described by Alexander et al. (2008). We take advantage of the deployment phase of the COSMIC constellation, when pairs of satellites were often physically close (Liou et al., 2007). During this phase, a single occulting GPS satellite was often tracked by a close pair of COSMIC satellites, resulting in a significant number pairs of profiles that were closely spaced and closely timed, with near-parallel lines of sight. These particular profile pairs permit the use of a k_H estimation method and subsequently an estimation of gravity wave momentum flux. k_H has also been determined in a similar manner in recent studies by McDonald (2012) and Faber et al. (2013) . In this section, we use this method to make estimates of gravity wave momentum flux from COSMIC

GPS-RO during June-August 2006 over the southern Andes, Drake Passage and Antarctic Peninsula.

4.1 Profile pair selection and processing

First, we identify profile pairs during June-August 2006 that are closely spaced, closely timed and have near-parallel lines of sight. We require that the two profiles must (1) be horizontally separated by less than 300 km at a height of 30 km; (2) be separated in time by less than 15 minutes; and (3) have lines of sight aligned within 30° of each other. The line of sight requirement is important since ~~the observational filter of GPS-RO requires that waves must have $\lambda_H \gtrsim 270$~~we require that waves have $\lambda_H \geqslant 270$ km in the line of sight as discussed in Section 1.1.1. If the two viewing angles differ by a large amount, ~~we may not resolve~~ the same wave might not be observable in both profiles. Finally, we require that a clear wave-like ~~signal~~ feature of approximately the same vertical wavelength (± 1.5 km) is identified in both profiles using the Wave-ID method described in section 3.1. A discussion of this vertical wavelength criterion as an identification method for the same wave in both profiles is provided by McDonald (2012) .

In practise, we find that the majority of profile pairs during June-August 2006 have horizontal separations ~~of 10-20~~$\sim$10 km (see Figure 12a), time separations of less than a minute and lines-of-sight separated by less than 1°. Hence requirements (1), (2) and (3) are usually satisfied. The requirement that both profiles contain the same wave-like ~~signal~~ feature reduces the number of available pairs from $\sim$~~21000~~ 75000 to $\sim$~~7000~~ 14000 globally during June-August 2006. Of these, around ~~900~~ 1300 lie in our geographical region of interest.

To estimate k_H in each profile pair, we follow a modified form of the method described by Alexander et al. (2008). We first apply a Gaussian window of FWHM = 22 km centred at 30 km altitude as described in section 3.1. We next compute the CWT of each profile.

The resulting transform $\tilde{T}(z, \lambda_Z)$ is a complex valued function of altitude z and vertical wavelength λ_Z. For the two profiles a and b, the cospectrum $C_{a,b}$ is computed as

$$C_{a,b} = \tilde{T}_a \tilde{T}_b^* = \hat{T}_a \hat{T}_b e^{i\Delta\phi_{a,b}} \tag{7}$$

where $\hat{T}$ is the magnitude and $\Delta\phi_{a,b}$ is the phase difference between the two profiles for each λ_Z at each position z. The covariance spectrum is the absolute value $|C_{a,b}|$. We locate the maximum in the covariance spectrum C_{max} in the height region 20-40 km, for vertical wavelengths less than 18 km. The location of C_{max} in the covariance spectrum corresponds to the dominant vertical wavelength λ_{DOM} common to both profiles at altitude z_{DOM}. We then compute the phase difference between the two profiles $\Delta\phi_{a,b}$ as

$$\Delta\phi_{a,b} = \arctan\left(\frac{\text{Im}(C_{a,b})}{\text{Re}(C_{a,b})}\right) \tag{8}$$

where $\text{Re}(C_{a,b})$ and $\text{Im}(C_{a,b})$ are the real and imaginary coefficients of the covariance spectrum $C_{a,b}$. We record the value of $\Delta\phi_{a,b}$ at C_{max}.

We then compute the projection of the horizontal wavenumber k_H along the horizontal axis joining the two profiles a and b as

$$k_H = \frac{\Delta\phi_{a,b}}{\Delta r_{a,b}} \tag{9}$$

where $\Delta r_{a,b}$ is the horizontal separation of profiles a and b at around 30 km altitude. We then compute $\lambda_H = 2\pi/k_H$. This projected value of λ_H is typically longer than the true horizontal wavelength, and hence represents an upper-bound estimate (Ern et al., 2004). A useful illustration of this geometry can be found in (Preusse et al., 2009) . We require that $100 \leqslant \lambda_H \leqslant 5000$ km to exclude unphysically short or extremely long horizontal wavelengths. This exclusion is discussed in more detail in Appendix A.

Generally, the horizontal separation Δr of our profile-pairs is much shorter than the LOS horizontal resolution $\Delta L \sim 270$ km. Therefore, any phase difference measured between the profiles is not likely to be the result of phase difference in the LOS direction, but the result of phase difference perpendicular to the LOS. For this reason we take Δr to be the perpendicular horizontal separation of the pair with respect to the LOS or the first profile in each pair. This is generally close to the absolute horizontal separation due to the geometry of the constellation during the deployment phase.

To obtain an estimate of wave amplitude T', we find the maximum amplitude in each ~~original perturbation profile a and b~~ perturbation profile $T'_a(z)$ and $T'_b(z)$ over the height region $z_{\text{DOM}} \pm \lambda_{\text{DOM}}/2$, and take the mean.

Finally we compute an estimate of the absolute value of momentum flux M_{flux} as

$$M_{\text{flux}} = \frac{\bar{\rho}}{2} \frac{\lambda_Z}{\lambda_H} \left(\frac{g}{N}\right)^2 \left(\frac{T'}{\bar{T}}\right)^2 \tag{10}$$

where $\bar{\rho}$ is local atmospheric density, g is acceleration due to gravity and N is the Brunt-Väisälä (buoyancy) frequency. ~~Here, since λ_H is an upper-bound estimate, Equation 10 represents a lower-bound estimate of gravity wave momentum flux (Alexander et al., 2008) .~~

4.2 COSMIC momentum flux results

Figure 10 shows gravity wave vertical wavelengths, horizontal wavelengths and momentum flux from our COSMIC pair analysis over the southern Andes, Drake Passage and Antarctic Peninsula during June-August 2006. Also shown are coincident results from HIRDLS, using the Stockwell Transform (S-Transform Stockwell et al., 1996) method described by Alexander et al. (2008) modified by Wright and Gille (2013). COSMIC and HIRDLS are sensitive to ~~different but~~ broadly overlapping parts of the gravity-wave spectrum, so we provide results from HIRDLS as a comparison.

In Figure 10a, our COSMIC analysis shows longer mean vertical wavelengths over the southern tip of South America extending south over the Drake Passage. This southward extension out over the Drake Passage is in good agreement with a case study of a large mountain wave event in the region by Alexander and Teitelbaum (2011), ~~though they inferred~~ using data from the Atmospheric InfraRed Sounder (AIRS) instrument. They did however infer longer vertical wavelengths due to the deep vertical weighting function of the AIRS instrument and the assumption of zero ground-based phase velocities. This region of longer vertical wavelength also extends further south over the Antarctic Peninsula.

The corresponding HIRDLS analysis in Figure 10d shows typically longer λ_Z values overall, likely due to the increased sensitivity of HIRDLS to waves with long λ_Z as a result of the larger usable height range in HIRDLS profiles. Like our COSMIC analysis, Figure 10d also shows longer mean vertical wavelengths over the southern tip of South America. However, a region of longer vertical wavelengths is also evident between 80-100°W that is not seen in our COSMIC analysis. We do not fully understand the reasons for this, but we suspect that it may be due to differing vertical wavelength sensitivities of HIRDLS and COSMIC. A full investigation into the distributions of vertical wavelengths from the HIRDLS S-Transform analysis is however beyond the scope of this study.

The results of our λ_H analysis from COSMIC profile-pairs is presented in Figure 10b. We mostly observe values of around 600-800 km, but no structured geographical pattern is evident. We suspect this distribution (or lack thereof) may be due to the viewing geometry of GPS-RO technique, more specifically the orientation of the horizontal axis joining the two profiles in each profile pair, which can vary significantly between pairs. Since the measured horizontal wavelength is the projection of the true λ_H along the axis between the two profiles, it is a upper-bound estimate heavily dependent the orientation of this horizontal axis. Even in a region where the wave field has a preferential horizontal alignment we will still recover a range of horizontal wavelength estimates due to differing orientations. HIRDLS scan-tracks are more consistently aligned ∼NW-SE or ∼NE-SW across this region, and hence estimates of λ_H between adjacent HIRDLS profiles will be more consistent, but not necessarily more accurate. This is likely the reason that the more structured geographical

distribution of λ_H shown in HIRDLS results, where shorter horizontal wavelengths are observed generally south and east of the southern tip of South America, is not observed by COSMIC.

The absolute values of our λ_H analysis are however physically reasonable and in good agreement with other studies such as Ern et al. (2004). ~~However, our~~ They are however much shorter than HIRDLS estimates. Our COSMIC profile-pairs typically have smaller horizontal ~~separation~~ separations (~~20~~10 km) between ~~adjacent profiles~~ profile-pairs than HIRDLS (~80 km for an ascending-descending pair, ~120 km for a descending-ascending pair (e.g. Wright et al., 2015)). This means that any ~~large positive~~ absolute error in phase difference $\Delta\phi_{a,b}$ between COSMIC pairs will bias our results towards shorter λ_H ~~by the relation in Equation 9~~than might be found in a HIRDLS profile-pair. We suspect that this may be the reason we observe ~~slightly~~ lower absolute horizontal wavelength values in our COSMIC analysis than in HIRDLS. The results are not contradictory however, since both estimates represent an upper-bound. This sensitivity to errors in phase difference and their effect on λ_H estimation with regards to horizontal separation is discussed more fully in Appendix A.

Figure 10c shows the results of our COSMIC momentum flux analysis. Two local maxima of order 10^{-2} Pa are observed over the southern tip of South America and the Antarctic Peninsula. This increased flux over the southern tip of South America is in good agreement with results from CRISTA (Ern et al., 2004) and HIRDLS (Alexander et al., 2008) and the maximum over the Antarctic Peninsula is in good agreement with results from the Vorcore superpressure balloon campaign presented in Hertzog et al. (2008). Hertzog et al. showed that most of the momentum flux in the maximum over the Antarctic Peninsula was in a westward direction, suggestive of orographic gravity waves propagating against the mean stratospheric flow. Increased momentum flux is also observed to the east of the two maxima, suggestive of significant wakes of associated gravity wave flux downwind from these sources.

The HIRDLS analysis Figure 10f shows a maximum over the southern tip of South America, consistent in location and magnitude with our COSMIC results. HIRDLS estimates of

gravity wave momentum flux are slightly higher, ~~but this is to be expected since HIRDLS generally resolves~~ though this could be somewhat expected since the HIRDLS analysis method used here generally resolved waves with longer ~~λ_z~~ vertical wavelengths than the COSMIC method. The COSMIC analysis is able to identify a secondary maximum over the Antarctic Peninsula which is not observed by HIRDLS due to the lack of measurements poleward of 62°S.

These momentum flux measurements reaffirm that the southern Andes and Antarctic Peninsula are intense and persistent sources of gravity wave momentum flux during austral winter. Perhaps more importantly however, our results demonstrate that, given sufficient sampling density, COSMIC GPS-RO can provide physically reasonable estimates of stratospheric gravity-wave momentum flux that are consistent with results from HIRDLS, CRISTA and Vorcore. The final configuration of the COSMIC constellation however restricts the number of suitable profile-pairs such that regional climatological studies of gravity wave momentum flux using our method are generally limited to the deployment phase in 2006. However, as discussed in Section 5, dramatically increased sampling density provided by upcoming radio occultation missions may provide an opportunity to apply this method on a global scale in coming years.

5 Discussion

During austral winter in the southern hemisphere, the mountains of the southern Andes and Antarctic Peninsula are a known hot spot of gravity wave fluxes (e.g. Alexander and Teitelbaum, 2007, 2011; Hoffmann et al., 2013). However, the origin of the long leeward distribution of enhanced gravity wave energy stretching eastwards far over the ocean is currently a topic for debate.

As discussed in Section 2.3, Sato et al. (2012) suggested that waves from the mountains of the southern tip of South America and northern tip of the Antarctic Peninsula can propagate significantly downwind if their horizontal wavenumber vectors are aligned at an acute angle to the mean stratospheric flow. However, using a ray-tracing analysis Sato et al. also

showed that for horizontal wavelengths of 250-350 km such waves rarely propagate east of the prime meridian, regardless of launch angle. Hence, the distribution of increased E_p shown here eastwards of around 20°E is not likely to be explained by the downwind propagation of waves with λ_H less than approximately 350 km. This suggests that the distribution of increased E_p eastwards of around 20°E may be the result of (1) downwind propagating mountain waves with λ_H > 350 km; (2) locally generated non-orographic waves from tropospheric or stratospheric sources out over the ocean; or (3) some combination of these processes.

Preusse et al. (2014) used backwards ray-tracing of resolved waves in ECMWF data to show that during August 2008, waves over the southern Andes and Antarctic Peninsula overwhelmingly had lowest traceable altitude (LTA) values close to the surface, whereas waves over the southern Atlantic and Indian oceans often had average LTA values around 7-12 km. Their results are indicative of upper-tropospheric non-orographic wave sources that exist out over the oceans. Similarly, Hendricks et al. (2014) suggested that a belt of increased stratospheric gravity wave activity observed by AIRS could be attributed to non-orographic sources in winter storm tracks around the southern Atlantic and Indian Oceans. ~~Our results presented in Figures 3 and 4 are not strongly suggestive of intense tropospheric non-orographic wave sources over the oceans, although these results do not explicitly preclude the existence of such sources. Furthermore,~~ The distribution of increased stratospheric E_p in our Figure 2 is morphologically reminiscent of southern hemisphere storms tracks in ECMWF ERA-40 data presented by Hoskins and Hodges (2005) , which may support the suggestion by Hendricks et al. . Our Figure 4 suggests that if waves from these sources significantly contribute to the region of increased stratospheric E_p over these oceans, then these waves generally have λ_Z too short ($\lesssim$ 3 km) to be resolved by COSMIC below ~20 km altitude. As these waves ascend, the mean wind speed increases and they might be refracted to longer vertical wavelengths such that they may be resolved and can contribute to the E_p in Figures 2 and 4. It should be noted however that the waves considered by Preusse et al. in ECMWF data are typically below the height region considered in this study, and the waves observed by Hendricks et al. in AIRS data are not typically

visible to ~~GPS-RO. We note, however, that the processes they describe may indeed have an influence on the distribution of E_p that we observe in COSMICdata~~COSMIC.

In Section 2.2 we presented evidence of a southward focussing of gravity waves into the centre of the stratospheric jet. In a recent modelling study, McLandress et al. (2012) showed that zonal wind biases and vortex breakdown timing errors in a latitude band near 60°S could be greatly reduced in the Canadian Middle Atmosphere Model (CMAM) through the inclusion of non-specific orographic gravity wave drag (GWD) in the stratosphere. One ~~hypotheses~~ hypothesis for the missing drag is unparametrized mountain waves from small islands in and around the Southern Ocean that are sub-gridscale in CMAM. A second hypothesis is the southward (northward) propagation of orographic waves from the north (south) into the southern stratospheric jet from outside the latitude band (McLandress et al., 2012; Our results ~~provide~~ suggest evidence of such meridional propagation. In particular, we observe a southward focusing of waves in Figure 3 into the jet around 60°W from sources further north, supporting the second hypothesis ~~of McLandress et al.~~ described above. It is conceivable that there exists a similar process whereby waves from the Antarctic Peninsula are focussed northwards into the jet, though we are unable to find such clear evidence for this in our results. Observational evidence of any meridional focusing is significant since many parametrization schemes used operationally in GCMs do not include such focussing phenomena (Preusse et al., 2014).

In Section 3 we investigated longitudinal variations in wave populations in the long leeward region of increased E_p during June-August 2006-2012. In regions immediately downwind of the southern Andes and Antarctic Peninsula we observe significantly more rare, large amplitude waves than in upwind regions, while only a slight increase in the absolute number of waves is observed. Further analysis (omitted for brevity) showed that exclusion of these large amplitude waves resulted in a much more zonally uniform distribution of mean wave energy around over the Southern Ocean. This suggests that the increased E_p observed immediately downwind of the mountains in Figure 7b is the result of increased numbers of rare, large amplitude wave events in this downwind region and not simply the result of more waves in general. As discussed in Section 3.2, this is consistent with the

results of a super-pressure balloon and modelling study by Hertzog et al. (2012). The eastward decrease in E_p values in Figure 7b correlates well to the eastward decrease of the frequency of occurrence of these rare, large amplitudes waves.

However, the general distributions of gravity wave amplitudes at all longitudes in the latitude band 40-65°S are broadly similar. This may be indicative of persistent, zonally uniform non-orographic source mechanisms in and around the stratospheric jet. Inertia-gravity waves, to which GPS-RO is preferentially sensitive, can often be generated at the edge of jet streams via spontaneous adjustment processes (Fritts and Alexander, 2003). Hence, a ~~significant~~ possible contribution to the long leeward region of increased E_p in Figure 7b may be from gravity waves generated via these adjustment mechanisms.

In the context of other studies, our results therefore suggest that the long leeward region of increased E_p consists of (1) rare, large amplitude waves over 80°W-40°E from orographic sources such as the southern Andes and Antarctic Peninsula that ~~have been focussed~~ may also have been meridionally-focussed and advected downwind; (2) a possible contribution secondary waves generated locally in the breaking region of these primary orographic waves; ~~and~~ (3) a possible contribution from non-orographic waves from sources associated with winter storm tracks over the southern oceans; and (4) a zonally uniform distribution of small amplitude waves from non-orographic mechanisms such as spontaneous adjustment and jet instability around the edge of the stratospheric jet. ~~A contribution from tropospheric non-orographic waves associated with storms around the southern Atlantic and Indian Oceans may also be present.~~

Finally, we described a method for the estimation of stratospheric gravity wave momentum flux from COSMIC GPS-RO. To our knowledge, there are very few studies that have successfully developed methodologies for gravity wave momentum flux estimates from GPS-RO data ~~(e.g. Wang and Alexander, 2010)~~ (e.g. Wang and Alexander, 2010; Faber et al., 20
Our results demonstrate that, given sufficient sampling density, COSMIC GPS-RO can produce physically reasonable estimates of stratospheric gravity wave momentum flux over the southern Andes and Antarctic Peninsula that are consistent with results from CRISTA, HIRDLS and Vorcore (Ern et al., 2004; Alexander et al., 2008; Hertzog et al., 2008). It

is important to note that our results have a bias towards shorter horizontal wavelength estimation for reasons discussed in Appendix A.

The method presented here is mostly limited to the deployment phase of the COSMIC constellation only, since the number of profile-pairs that satisfy the requirements outlined in Section 4.1 is very low once the satellites reached their final configuration.

However, GPS-RO is an expanding technique, with new missions scheduled for launch in the next decade. The 12-satellite COSMIC-2 constellation (Cook et al., 2013) will boast more than 8000 soundings per day, measuring the occultations of satellites from the European navigation satellite system GALILEO and the Russian Global Navigation Satellite System (GLONASS), in addition to the American GPS satellite constellation. COSMIC-2 will feature two deployment phases from which large numbers of closely spaced profile-pairs can be expected. Furthermore, the number of profile-pairs available from their final configuration is likely to increase significantly and there will be increased coverage in the tropics as a result of 6 low-inclination (24°) satellites.

6 Summary and Conclusions

In ~~the present studywe use~~ this study, we have used dry atmospheric temperature profiles from COSMIC GPS-RO to investigate gravity wave activity in the southern stratospheric hot spot around the southern Andes and Antarctic Peninsula. ~~We also investigate the long leeward region of increased E_p stretching out over the southern oceans during austral winter. In the hot spot~~ The new wavelet analysis technique we have presented allows identification of the properties of individual gravity waves, which we have used the determine gravity wave energies, amplitudes, momentum fluxes and variability.

In the hot-spot region, we ~~present evidence that indicates a southward focusing~~ have found clear evidence of the southward propagation of orographic gravity waves into the strong winds of the southern stratospheric jet. ~~These waves appear to come from sources far to the north during August 2010.~~ This phenomenon has been predicted by recent high-resolution modelling studies (e.g. Watanabe et al., 2008; Sato et al., 2009, 2012).

~~Our results~~We also investigated the long leeward region of increased E_p stretching out over the southern oceans during austral winter. Our results suggest that this region is the result of waves from a number of overlapping orographic and non-orographic sources.

Our results, in the context of other studies, suggest that the long leeward region of increased E_p is the result of waves from a number of overlapping orographic and non-orographic wave sources.

~~Large mean E_p~~ We have used the distribution of the amplitudes of individual waves to suggest that the large mean Ep values observed immediately downwind of the southern Andes and Antarctic Peninsula ~~are attributed to~~ result from an increased number of rare, large amplitude mountain waves that have propagated downwind via the ~~meachanism~~ mechanism described by Sato et al. (2012). The remaining distribution is likely to be the result of waves from a variety of non-orographic sources such as storms in and around the Southern Ocean (Hendricks et al., 2014; Preusse et al., 2014) and spontaneous adjustment mechanisms around the edge of the southern stratospheric jet (Fritts and Alexander, 2003; Hei et al., 2008).

We ~~also describe~~ have also described a method for the estimation of k_H from closely spaced pairs of COSMIC profiles measured during the deployment phase of the constellation in July-August 2006. We ~~show~~ have also shown that, given sufficient sampling density, estimations of gravity wave momentum flux in the region around the southern Andes and Antarctic Peninsula can be retrieved from COSMIC GPS-RO. These measurements are broadly consistent with results from CRISTA (Ern et al., 2004), HIRDLS (Alexander et al., 2008), and Vorcore (Hertzog et al., 2008). In the coming years, the increased sampling density offered by new GPS-RO missions may allow our approach to be temporally and geographically expanded, potentially providing estimates of stratospheric gravity wave momentum flux on a much wider scale.

Acknowledgements. This study is ~~generously~~ supported by the UK Natural Environment Research Council (NERC): CJW and NJM are supported by NERC grant NE/K015117/1 and NPH by a PhD studentship awarded to the University of Bath. We are grateful to Andrew Moss for helpful sug-

gestions and discussions. We would also like to acknowledge Harrower and Brewer (2003) for the ColorBrewer colormaps featured in this study.

Appendix A: On the determination of λ_H from COSMIC profile-pairs

The increased number of closely-spaced profile-pairs during the deployment phase of the COSMIC constellation facilitates a focussed momentum flux study in the hot spot region. Many of these profile-pairs have very short horizontal separations $\Delta r \sim 10$ km. The method for the estimation of λ_H described in Section 4.1 is inherently sensitive to error in the determination of vertical phase shift $\Delta\phi$. The short horizontal separation of these pairs may introduce a bias towards shorter horizontal wavelengths. Other than comparing our λ_H estimates to estimates from other studies as in Section 4.2, it is difficult to independently quantify the error and reliability of these estimates. This Appendix discusses the effect of short horizontal separations of COSMIC profile-pairs on the estimation of λ_H in comparison to profile-pairs from the HIRDLS mission.

A1 Horizontal profile-pair separations

An estimate of horizontal wavelength λ_H can be calculated from the horizontal separation and phase difference between two adjacent profile-pairs via the relation in Equation 9. For a given wave field, it would be expected that in general, shorter horizontal separations between profile-pairs would result in smaller phase differences in profile-pairs.

Along the HIRDLS scan-track, vertical profiles are measured in an alternating "upscan" and "downscan" pattern. An illustration of this pattern can be seen in Wright et al. (2015, their Fig. 2). At an altitude of 30 km, alternating "downscan/upscan (D/U) and "upscan/downscan" (U/D) profile-pairs have horizontal separations of ∼80 km and ∼120 km respectively (see blue bars in our Figure 12a).

Figure 11 shows histograms of gravity wave phase differences between COSMIC, HIRDLS D/U and HIRDLS U/D profile-pairs during June-August 2006. Planetary wave features were removed from COSMIC profiles via a zonal high-pass filtering method, suppressing zonal

wavenumbers $s \leqslant 6$. HIRDLS profile-pairs are processed using the method described by Wright and Gille (2013) .

All three horizontal separations in Figure 11 indicate a general preference towards small ($\Delta\phi < \frac{\pi}{8}$) phase differences. To investigate the relative differences between each of the distributions, we normalise each histogram such that the total number of profiles in each is equal to one. We then subtract each normalised distribution from the mean of the three to find the relative difference. The bottom panel of Figure 11 indicates that COSMIC pairs with $\Delta r \sim 10$ km generally have more small ($\Delta\phi < \frac{\pi}{8}$) and fewer large ($\Delta\phi > \frac{\pi}{8}$) phase difference values than HIRDLS pairs. The HIRDLS U/D pairs, with the largest horizontal separation, generally have more large phase differences.

This suggests that, as might be expected, shorter horizontal separations between profile-pairs generally result in smaller phase differences. This result provides a useful sanity-check for the λ_H estimation methodology, particularly its application to COSMIC profile-pairs.

A2 Biases from small phase differences

Even if the methodology is valid for horizontal separations as short as $\sim$10 km, error in the determination of $\Delta\phi$ will have a larger effect, since the method is more reliant on the determination of very small phase differences. If the absolute error in determination of $\Delta\phi$ is $\pm 0.1 \approx \frac{\pi}{30}$ radians, then absolute phase differences of $0 \leqslant \Delta\phi \leqslant \frac{\pi}{30}$ will be indistinguishable from each other. For a COSMIC profile-pair with $\Delta r \sim$10 km, horizontal wavelengths greater than 600 km projected along the axis joining the profile-pair would therefore be ambiguous due to this error.

The shortest theoretically resolvable horizontal wavelength from a COSMIC profile-pair is twice the horizontal separation, $2 \times \Delta r \approx$20 km. However, the requirement of $\lambda_H \gtrsim$270 km in the LOS direction implies the rare case where the LOS is very closely aligned perpendicular to the horizontal wavenumber vector. Therefore large numbers of these very short λ_H estimates are unlikely to be physical, and an approximate cut-off of $\lambda_H \gtrsim 100$ km may be more realistic.

For an absolute error in phase difference of $\pm\frac{\pi}{30}$, λ_H estimates from COSMIC profile-pairs with $\Delta r \sim 10$ km may be accurate for $100 \lesssim \lambda_H \lesssim 600$ km. For larger horizontal separations and/or more accurate phase difference determinations, the upper limit is larger. Figure 12d shows a density plot of horizontal separation against phase difference for COSMIC profile-pairs in which a wave was identified via the method described in Section 3. Dashed black lines show lines of constant λ_H estimated via the relation in Equation 9. For the majority of detected waves $250 \lesssim \lambda_H \lesssim 5000$ km. A low-bias effect on the estimation of λ_H for short horizontal separations $\Delta r \sim 10$ km due to the error in the determination $\Delta\phi$ can be seen in the bottom left corner of the panel.

In summary, we suggest that phase difference estimates from COSMIC profile-pairs from the deployment phase of the constellation are broadly in line with what we might expect when compared to HIRDLS profile-pairs. However, the typically short horizontal separations of the closely spaced COSMIC profile-pairs used in Section 4 are likely to introduce a low-bias in the estimation of λ_H due to error in the determination of $\Delta\phi$. We suspect that this is the reason for the differences in λ_H estimates between COSMIC and HIRDLS in Figure 10e. The estimates are not necessarily contradictory, since both represent an upper bound value, but this bias should be considered when comparing results from the two instruments.

References

Alexander, M. J. and Barnet, C.: Using satellite observations to constrain parameterizations of gravity wave effects for global models., Journal of the Atmospheric Sciences, 64, 1652–1665, doi:10.1175/JAS3897.1, 2007.

Alexander, M. J. and Grimsdell, A. W.: Seasonal cycle of orographic gravity wave occurrence above small islands in the Southern Hemisphere: Implications for effects on the general circulation, Journal of Geophysical Research, 118, 11 589–11 599, doi:10.1002/2013JD020526, 2013.

Alexander, M. J. and Teitelbaum, H.: Observation and analysis of a large amplitude mountain wave event over the Antarctic peninsula, Journal of Geophysical Research, 112, doi:10.1029/2006JD008368, 2007.

Alexander, M. J. and Teitelbaum, H.: Three-dimensional properties of Andes mountain waves observed by satellite: A case study, Journal of Geophysical Research, 116, doi:10.1029/2011JD016151, 2011.

Alexander, M. J., Gille, J., Cavanaugh, C., Coffey, M., Craig, C., Eden, T., Francis, G., Halvorson, C., Hannigan, J., Khosravi, R., Kinnison, D., Lee, H., Massie, S., Nardi, B., Barnett, J., Hepplewhite, C., Lambert, a., and Dean, V.: Global estimates of gravity wave momentum flux from High Resolution Dynamics Limb Sounder observations, Journal of Geophysical Research, 113, D15S18, doi:10.1029/2007JD008807, 2008.

Alexander, M. J., Eckermann, S. D., Broutman, D., and Ma, J.: Momentum flux estimates for South Georgia Island mountain waves in the stratosphere observed via satellite, Geophysical Research Letters, 36, L12 816, doi:10.1029/2009GL038587, 2009.

Alexander, M. J., Geller, M., McLandress, C., Polavarapu, S., Preusse, P., Sassi, F., Sato, K., Eckermann, S., Ern, M., Hertzog, A., Kawatani, Y., Pulido, M., Shaw, T. A., Sigmond, M., Vincent, R., and Watanabe, S.: Recent developments in gravity-wave effects in climate models and the global distribution of gravity-wave momentum flux from observations and models, Quarterly Journal of the Royal Meteorological Society, 136, 1103–1124, doi:10.1002/qj.637, 2010.

Alexander, P. and de la Torre, A.: A method to improve the determination of wave perturbations close to the tropopause by using a digital filter, Atmospheric Measurement Techniques, 4, 1777–1784, doi:10.5194/amt-4-1777-2011, 2011.

Alexander, S. P., Tsuda, T., Kawatani, Y., and Takahashi, M.: Global distribution of atmospheric waves in the equatorial upper troposphere and lower stratosphere: COSMIC observations of wave mean flow interactions, Journal of Geophysical Research, 113, doi:10.1029/2008JD010039, 2008.

Alexander, S. P., Klekociuk, A. R., and Tsuda, T.: Gravity wave and orographic wave activity observed around the Antarctic and Arctic stratospheric vortices by the COSMIC GPS-RO satellite constellation, Journal of Geophysical Research, 114, doi:10.1029/2009JD011851, 2009.

Bacmeister, J. T. and Schoeberl, M. R.: Breakdown of Vertically Propagating Two-Dimensional Gravity Waves Forced by Orography, Journal of the Atmospheric Sciences, 46, 2109–2134, 1989.

Cook, K., Fong, C. J., Yen, N., Wenkel, M. J., Wilezynski, P., and Chang, G. S.: FORMOSAT-7/COSMIC-2 GNSS radio occultation constellation mission for global weather monitoring, IEEE Aerospace Conference, doi:10.1109/AERO.2013.6497317, 2013.

Eckermann, S. D. and Preusse, P.: Global Measurements of Stratospheric Mountain Waves from Space, Science, 286, 1534–1537, doi:10.1126/science.286.5444.1534, 1999.

Ern, M., Preusse, P., Alexander, M. J., and Warner, C. D.: Absolute values of gravity wave momentum flux derived from satellite data, Journal of Geophysical Research, 109, D20 103, doi:10.1029/2004JD004752, 2004.

Faber, A., Llamedo, P., Schmidt, T., de la Torre, A., and Wickert, J.: On the determination of gravity wave momentum flux from GPS radio occultation data, Atmospheric Measurement Techniques, 6, 3169–3180, doi:10.5194/amt-6-3169-2013, 2013.

Fjeldbo, G., Kliore, A. J., and Eshlemen, V. R.: Neutral Atmosphere of Venus as studied with Mariner-V radio occultation experiments, The Astronomical Journal, 76, 123–140, doi:10.1086/111096, 1971.

Fritts, D. C. and Alexander, M. J.: Gravity wave dynamics and effects in the middle atmosphere, Reviews of Geophysics, 41, 1003, doi:10.1029/2001RG000106, 2003.

Geller, M., Alexander, M. J., Love, P., Bacmeister, J., Ern, M., Hertzog, A., Manzini, E., Preusse, P., Sato, K., Scaife, A., and Zhou, T.: A Comparison between Gravity Wave Momentum Fluxes in Observations and Climate Models, Journal of Climate, 26, 6383–6405, doi:10.1175/JCLI-D-12-00545.1, 2013.

Gong, J., Wu, D. L., and Eckermann, S. D.: Gravity wave variances and propagation derived from AIRS radiances, Atmospheric Chemistry and Physics, 12, 1701–1720, doi:10.5194/acp-12-1701-2012, 2012.

Harrower, M. and Brewer, C.: ColorBrewer.org: An Online Tool for Selecting Colour Schemes for Maps, The Cartographic Journal, 40, 27–37, doi:10.1179/000870403235002042, 2003.

Hei, H., Tsuda, T., and Hirooka, T.: Characteristics of atmospheric gravity wave activity in the polar regions revealed by GPS radio occultation data with CHAMP, Journal of Geophysical Research, 113, D04 107, doi:10.1029/2007JD008938, 2008.

Hendricks, E., Doyle, J., Eckermann, S. D., Jiang, Q., and Reinecke, P.: What Is the Source of the Stratospheric Gravity Wave Belt in Austral Winter?, Journal of the Atmospheric Sciences, 71, 1583–1592, doi:10.1175/JAS-D-13-0332.1, 2014.

Hertzog, A., Boccara, G., Vincent, R. A., Vial, F., and Cocquerez, P.: Estimation of gravity wave momentum flux and phase speeds from quasi-Lagrangian stratospheric balloon flights. Part II: Results from the Vorcore campaign in Antarctica., Journal of the Atmospheric Sciences, 65, 3056–3070, doi:10.1175/2008JAS2710.1, 2008.

Hertzog, A., Alexander, M. J., and Plougonven, R.: On the Intermittency of Gravity Wave Momentum Flux in the Stratosphere, Journal of the Atmospheric Sciences, 69, 3433–3448, doi:10.1175/JAS-D-12-09.1, 2012.

Hoffmann, L., Xue, X., and Alexander, M. J.: A global view of stratospheric gravity wave hotspots located with Atmospheric Infrared Sounder observations, Journal of Geophysical Research: Atmospheres, 118, 416–434, doi:10.1029/2012JD018658, 2013.

Hoskins, B. and Hodges, K.: A new perspective on Southern Hemisphere storm tracks, Journal of Climate, 18, 4108–4129, doi:10.1175/JCLI3570.1, 2005.

Kursinski, E. R., Hajj, G. A., Schofield, J. T., Linfield, R. P., and Hardy, K. R.: Observing Earth's atmosphere with radio occultation measurements using the Global Positioning System, Journal of Geophysical Research, 102, 23 429–23 465, doi:10.1029/97JD01569, 1997.

Liou, Y. A., Pavelyev, A. G., Pavelyev, A. A., Yen, N., Huang, C. Y., and Fong, C. J.: FORMOSAT-3/COSMIC GPS radio occultation mission: Preliminary results, IEEE Transactions on Geoscience and Remote Sensing, 45, 3813–3826, 2007.

Marquardt, C. and Healy, S.: Measurement noise and stratospheric gravity wave characteristics obtained from GPS occultation data, Journal of the Meteorological Society of Japan, 83, 417–428, doi:10.2151/JMSJ-83-417, 2005.

McDonald, A. J.: Gravity wave occurrence statistics derived from paired COSMIC/FORMOSAT3 observations, Journal of Geophysical Research, 117, D15 106, doi:10.1029/2011JD016715, 2012.

McLandress, C., Shepherd, T. G., Polavarapu, S., and Beagley, S. R.: Is Missing Orographic Gravity Wave Drag near 60°S the Cause of the Stratospheric Zonal Wind Biases in Chemistry–Climate Models?, Journal of the Atmospheric Sciences, 69, 802–818, doi:10.1175/JAS-D-11-0159.1, 2012.

O'Sullivan, D. and Dunkerton, T. J.: Generation of inertia-gravity waves in a simulated life-cycle of baroclinic instability, Journal of the Atmospheric Sciences, 52, 3695–3716, doi:10.1175/1520-0469(1995)052<3695:GOIWIA>2.0.CO;2, 1995.

Plougonven, R., Hertzog, A., and Guez, L.: Gravity waves over Antarctica and the Southern Ocean: consistent momentum fluxes in mesoscale simulations and stratospheric balloon observations, Quarterly Journal of the Royal Meteorological Society, 139, 101–118, doi:10.1002/qj.1965, 2013.

Preusse, P., Doernbrack, A., and Eckermann, S.: Space-based measurements of stratospheric mountain waves by CRISTA 1. Sensitivity, analysis method, and a case study, Journal of Geophysical Research, 107, 8178, doi:10.1029/2001JD000699, 2002.

Preusse, P., Eckermann, S. D., and Ern, M.: Transparency of the atmosphere to short horizontal wavelength gravity waves, Journal of Geophysical Research, 113, D24 104, doi:10.1029/2007JD009682, 2008.

Preusse, P., Schroeder, S., Hoffmann, L., Ern, M., Friedl-Vallon, F., Ungermann, J., Oelhaf, H., Fischer, H., and Riese, M.: New perspectives on gravity wave remote sensing by spaceborne infrared limb imaging, Atmospheric Measurement Techniques, 2, 299–311, doi:10.5194/amt-2-299-2009, 2009.

Preusse, P., Ern, M., Bechtold, P., Eckermann, S. D., Kalisch, S., Trinh, Q. T., and Riese, M.: Characteristics of gravity waves resolved by ECMWF, Atmospheric Chemistry and Physics, 14, doi:10.5194/acp-14-10483-2014, 2014.

Sato, K., Watanabe, S., Kawatani, Y., Tomikawa, Y., Miyazaki, K., and Takahashi, M.: On the origins of mesospheric gravity waves, Geophysical Research Letters, 36, L19 801, doi:10.1029/2009GL039908, 2009.

Sato, K., Tateno, S., Watanabe, S., and Kawatani, Y.: Gravity Wave Characteristics in the Southern Hemisphere Revealed by a High-Resolution Middle-Atmosphere General Circulation Model., Journal of the Atmospheric Sciences, 69, 1378–1396, doi:10.1175/JAS-D-11-0101.1, 2012.

Savitzky, A. and Golay, M. J. E.: Smoothing and Differentiation of Data by Simplified Least Squares Procedures, Analytical Chemistry, 36, 1627–1639, 1964.

Scaife, A., Butchart, N., Warner, C., Stainforth, D., Norton, W., and Austin, J.: Realistic quasi-biennial oscillations in a simulation of the global climate, Geophysical Research Letters, 27, 3481–3484, doi:10.1029/2000GL011625, 2000.

Stockwell, R., Mansinha, L., and Lowe, R. P.: Localization of the complex spectrum: the S-Transform, IEEE Transactions on Signal Processing, 44, 998–1001, 1996.

Tsuda, T., Lin, X., Hayashi, H., and Noersomadi: Analysis of vertical wave number spectrum of atmospheric gravity waves in the stratosphere using COSMIC GPS radio occultation data, Atmospheric Measurement Techniques, 4, 1627–1636, doi:10.5194/amt-4-1627-2011, 2011.

Wang, L. and Alexander, M. J.: Global estimates of gravity wave parameters from GPS radio occultation temperature data, Journal of Geophysical Research, 115, D21 122, doi:10.1029/2010JD013860, 2010.

Watanabe, S., Kawatani, Y., Tomikawa, Y., Miyazaki, K., Takahashi, M., and Sato, K.: General aspects of a T213L256 middle atmosphere general circulation model, Journal of Geophysical Research, 113, D12 110, doi:10.1029/2008JD010026, 2008.

Wright, C. J. and Gille, J. C.: HIRDLS observations of gravity wave momentum fluxes over the monsoon regions, Journal of Geophysical Research, 116, doi:10.1029/2011JD015725, 2011.

Wright, C. J. and Gille, J. C.: Detecting overlapping gravity waves using the S-Transform, Geophysical Research Letters, 40, 1850–1855, doi:10.1002/grl.50378, 2013.

Wright, C. J., Osprey, S. M., and Gille, J. C.: Global observations of gravity wave intermittency and its impact on the observed momentum flux morphology, Journal of Geophysical Research: Atmospheres, 118, 10,980–10,993, doi:10.1002/jgrd.50869, 2013.

Wright, C. J., Osprey, S. M., and Gille, J. C.: Global distributions of overlapping gravity waves in HIRDLS data, Atmospheric Chemistry and Physics Discussions, pp. 4333–4382, doi:10.5194/acpd-15-4333-2015, 2015.

Wu, D. L. and Jiang, J. H.: MLS observations of atmospheric gravity waves over Antarctica, Journal of Geophysical Research, 107, 4773, doi:10.1029/2002JD002390, 2002.

Wu, D. L. and Waters, J. W.: Satellite observations of atmospheric variances: A possible indication of gravity waves, Geophysical Research Letters, 23, 3631–3634, doi:10.1029/96GL02907, 1996.

Yan, X., Arnold, N., and Remedios, J.: Global observations of gravity waves from High Resolution Dynamics Limb Sounder temperature measurements: A year-long record of temperature amplitude, Journal of Geophysical Research, 115, D10 113, doi:10.1029/2008JD011511, 2010.

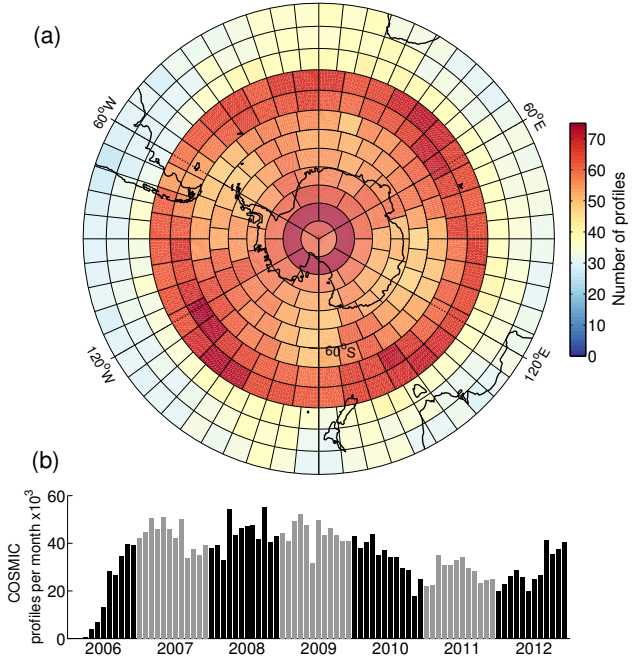

Figure 1. Polar stereographic projection of monthly-mean COSMIC sampling density for the period 2007-2012 (a), and total number of ~~occultaions~~ occultations per month for the period 2006-2012 (b). Each box in (a) represents an equal area of approximately 550 km^2. Alternating years in (b) are shown by black and gray bars.

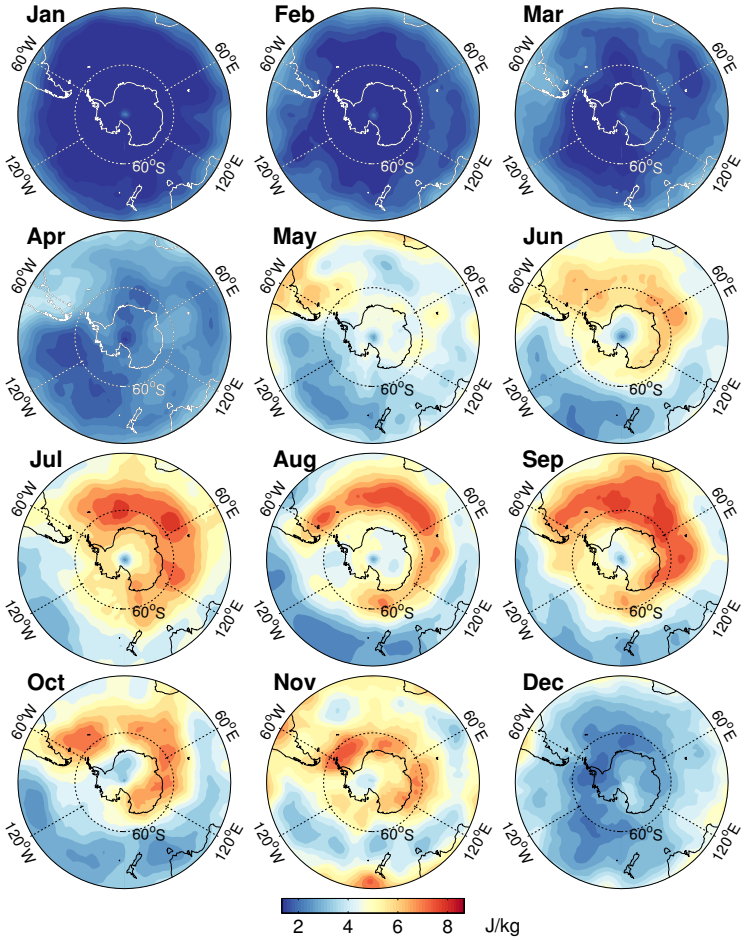

Figure 2. Polar stereo projections of monthly-mean potential energy per unit mass E_p in the southern hemisphere averaged over the height range 26-36 km (∼20-5 hPa) for each month in 2010.

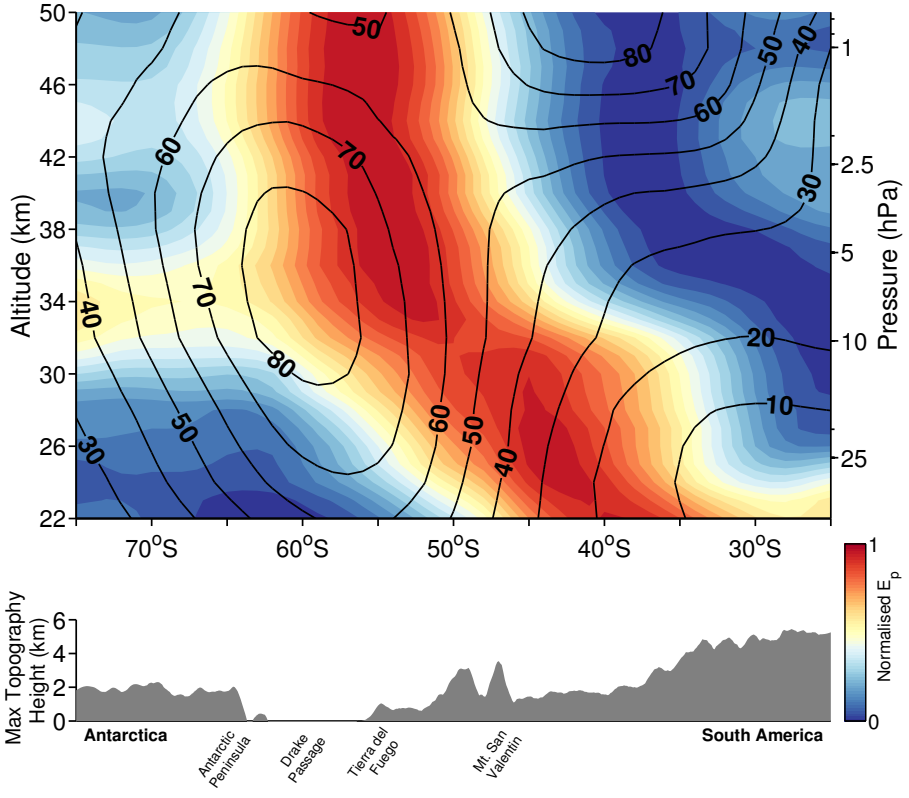

Figure 3. Normalised monthly-mean meridional cross-section of E_p in August 2010 over the southern Andes and Antarctic Peninsula (top panel) and maximum topography height (bottom panel) in a $\pm 5^\circ$ slice centred on 65°W. Monthly-mean zonal-mean winds from ECMWF operational analyses are shown by thick contours in the top panel, at intervals of 10 m/s. Note the E_p has been normalised at each height level to highlight the vertical structure.

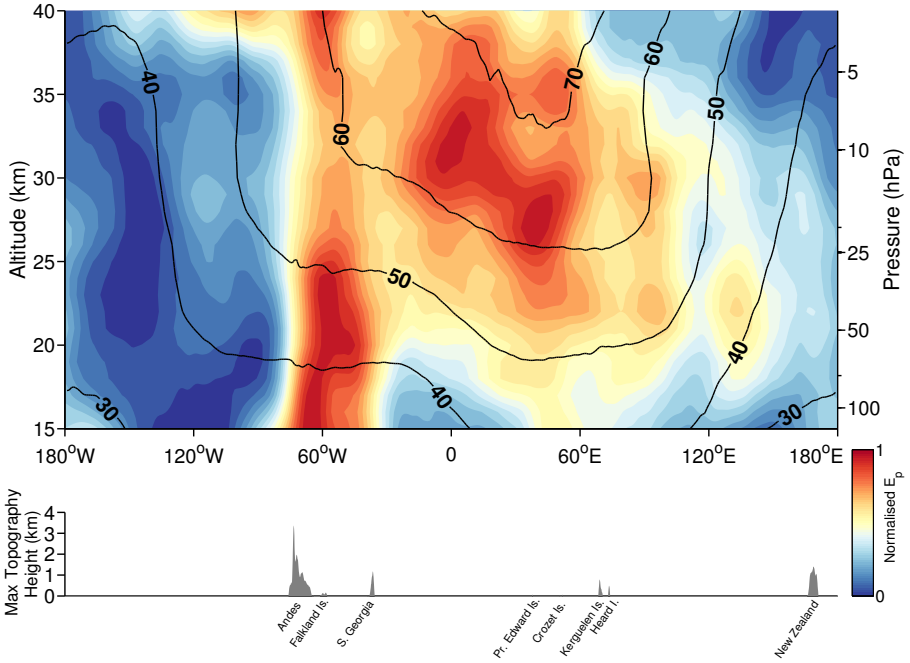

Figure 4. Normalised monthly mean zonal cross-section of E_p for August 2010 over Southern Ocean (top panel) and maximum topography height (bottom panel) in a $\pm 10^{\circ}$ slice centred on 50°S. Monthly mean zonal mean winds from ECMWF operational analyses are shown by thick contours in the top panel, at intervals of 10 m/s. Note the E_p has been normalised at each height level to highlight the vertical structure.

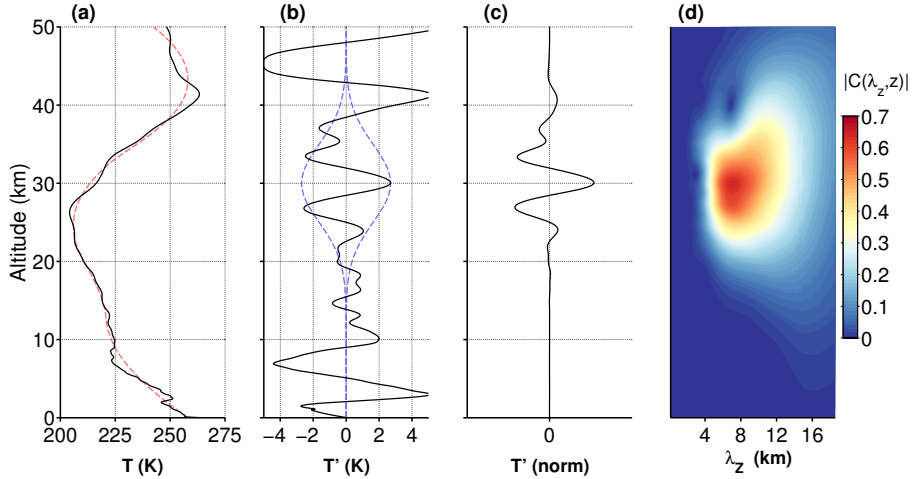

Figure 5. ~~Processing chain for wave~~ Wave identification ~~in a~~ (Wave-ID) methodology for an example COSMIC profile at 2319 UTC on 1st August 2010 at 53°S, 50°W. Panels show (a) raw temperature profile T (black solid) and filtered background temperature profile $\bar{T}$ (red dashed), (b) Temperature perturbation profile T' (black solid) and a Gaussian window centred on 30 km (blue dashed), (c) ~~root-sum-square~~ windowed, RSS normalised and ~~windowed~~ zero-averaged perturbation profile T'_{norm}, (d) ~~squared covariance spectrum~~ magnitudes of the ~~CWT~~ spectral coefficients of the ~~profile in (c)~~Continuous Wavelet Transform of T'_{norm}. For details, see text.

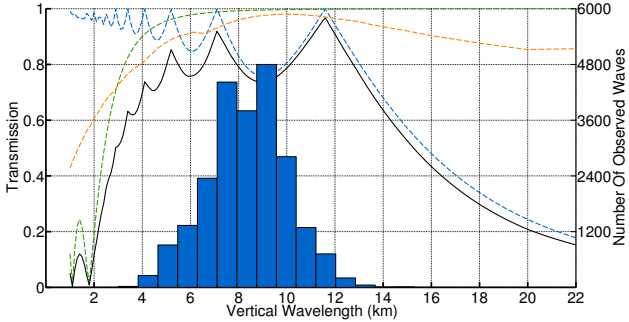

Figure 6. Transmission against vertical wavelength for each step in our Wave-ID processing for synthetic waves with λ_Z < 22 km centred at 30 km altitude: background subtraction (blue dashed); noise reduction (green dashed); Gaussian windowing and CWT (orange dashed); and the combined transmission (black solid). Blue bars show a histogram (right axis) of number of waves identified in COSMIC data in the region 35-75°S 0-90°W during June-August 2006-2012 using this method.

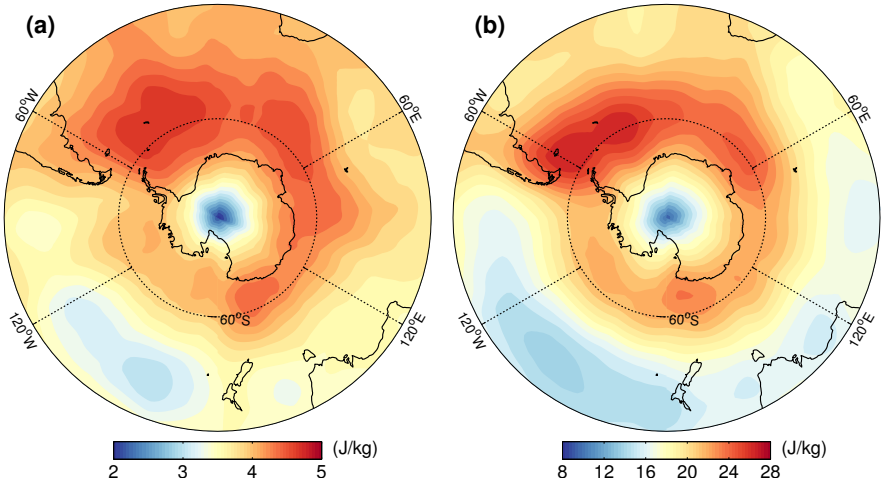

Figure 7. Polar stereo projections of E_p at 30 km ($\sim$10 hPa) for June-August 2006-2012 using (a) all available COSMIC profiles and (b) only individually identified waves using the Wave-ID method (see text).

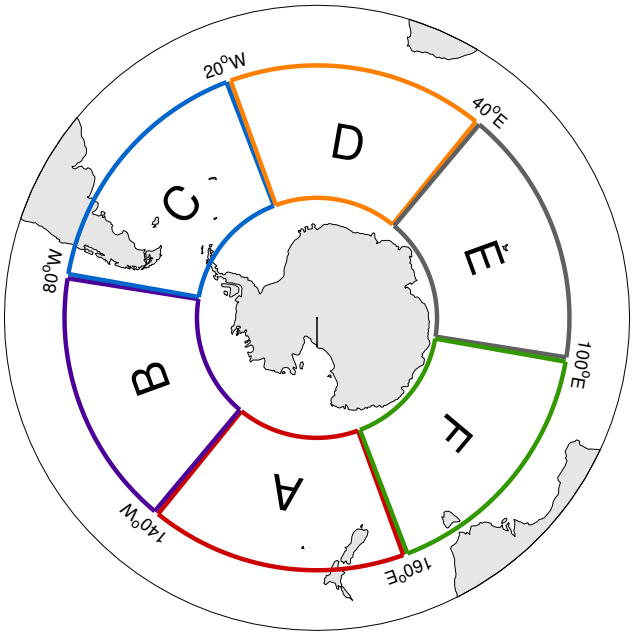

Figure 8. Polar stereo projection showing longitudinal Sectors A-F in the latitude band 40-65°S used in Figure 9.

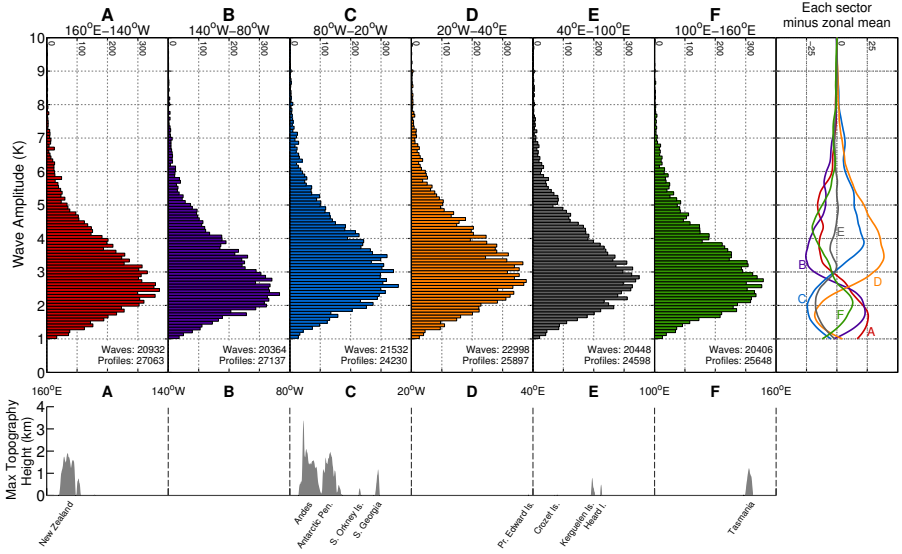

Figure 9. Histograms of individual wave amplitudes detected during June-August 2006-2012 in longitudinal sectors A-F in the latitude band 40-65°S using the Wave-ID method (see text). The rightmost panel shows the difference between the wave amplitude distribution in each sector and the zonal-mean distribution. The bottom panel shows maximum topography height in the latitude band 40-65°S

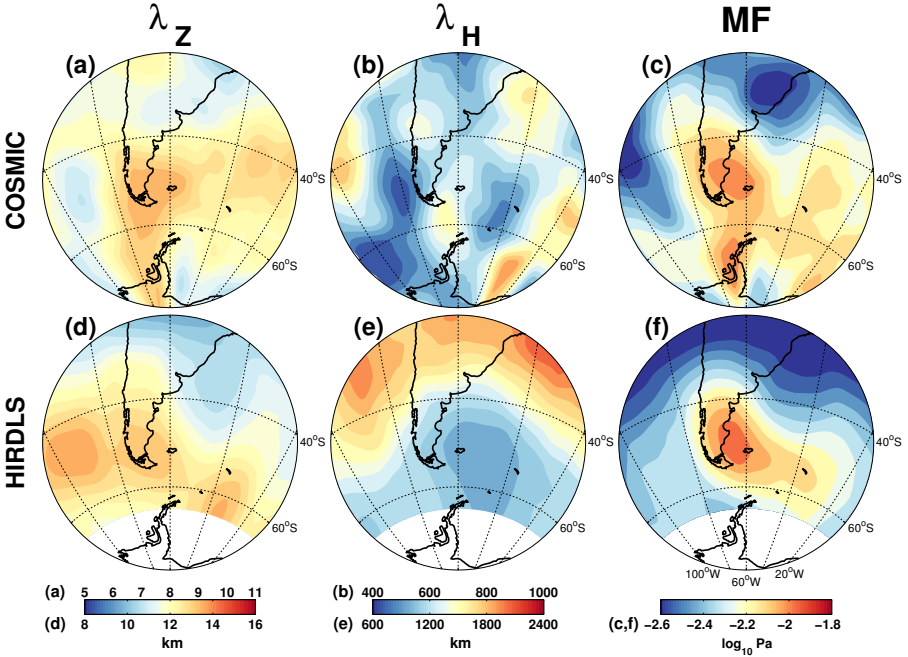

Figure 10. Orthographic projections of vertical wavelength λ_Z, horizontal wavelength λ_H and momentum flux (MF) for COSMIC (a,b,c) and HIRDLS (d,e,f) at 30 km (∼10 hPa) during June-August 2006.

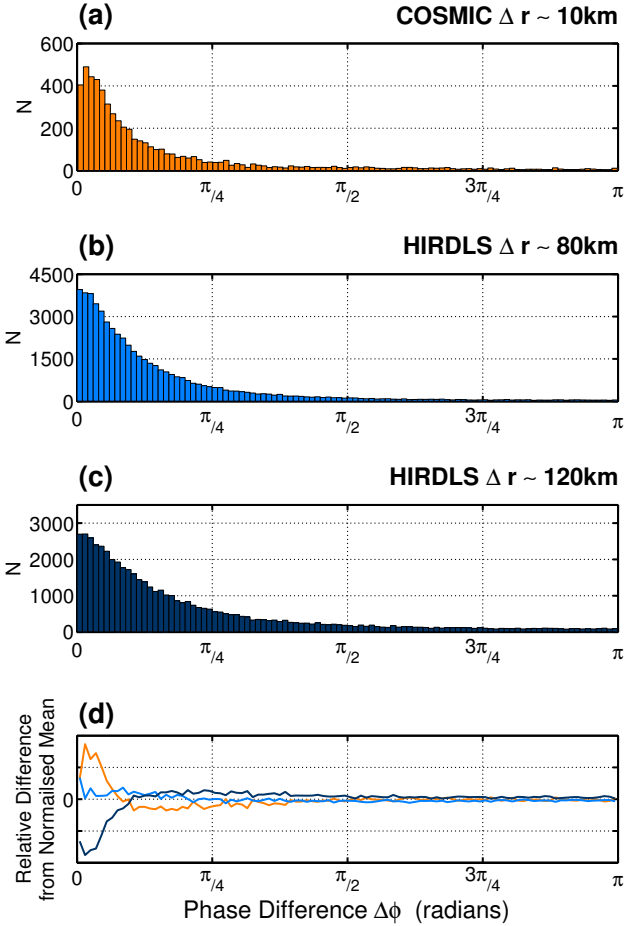
(a)
COSMIC Δ r ~ 10km
600
400
200
0
N
0
π/4
π/2
3π/4
π
(b)
HIRDLS Δ r ~ 80km
4500
3000
1500
0
N
0
π/4
π/2
3π/4
π
(c)
HIRDLS Δ r ~ 120km
3000
2000
1000
0
N
0
π/4
π/2
3π/4
π
(d)
Relative Difference
from Normalised Mean
0
0
π/4
π/2
3π/4
π
Phase Difference Δϕ (radians)

Figure 11. Histograms of gravity wave phase difference $\Delta\phi$ in (a) COSMIC profile-pairs, (b) HIRDLS "downscan-upscan" profile-pairs and (c) HIRDLS "upscan-downscan" profile-pairs globally during JJA 2006. Bottom panel (d) shows normalised relative difference of COSMIC (orange), HIRDLS downscan-upscan (light blue) and HIRDLS upscan-downscan (dark blue) from the mean of all three.

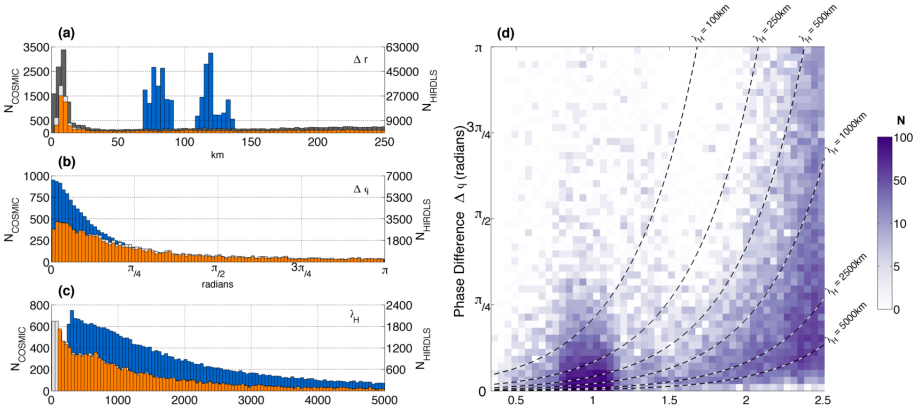

Figure 12. Number of COSMIC (N_{COSMIC}, orange and grey bars) and HIRDLS (N_{HIRDLS}, blue bars) profile-pairs against (a) horizontal separation Δr (b) phase difference $\Delta\phi$ and (c) projected horizontal wavelength λ_H globally for June-August 2006. Dark grey bars in (a) correspond to all available COSMIC profile-pairs. Light grey bars in (a,b,c) correspond to COSMIC profile-pairs in which a coherent wave was identified via the Wave-ID method. Orange bars in (a,b,c) correspond to COSMIC profile-pairs in which a wave was identified with $100 < \lambda_H < 5000$ km. Panel (d) shows a density plot of number of COSMIC profile-pairs N against horizontal separation and phase difference. Dashed black lines of constant λ_H are found via the relation in Eqn. 9.